A tunable structural family with ultralow thermal conductivity: copper deficient Cu1-x□xPb1-xBi1+xS3

Article

Accepted Version

A tunable structural family with ultralow thermal conductivity: copper deficient Cu1-x□xPb1-xBi1+xS3

Journal:	*Journal of the American Chemical Society*
Manuscript ID	ja-2021-11998c.R1
Manuscript Type:	Article
Date Submitted by the Author:	16-Dec-2021
Complete List of Authors:	Maji, Krishnendu; CRISMAT Lemoine, Pierric; Universite de Rennes 1, Institut des Sciences Chimiques de Rennes UMR-CNRS 6226 Renaud, Adèle; Institut des Sciences Chimiques de Rennes, Zhang, Bin; Chongqing University, Analytical and Testing Center Zhou, Xiaoyuan; colleges of physics of Chong Qing University, Carnevali, Virginia; Central Michigan University Candolfi, Christophe; Institut Jean Lamour, Chemistry and Physics of Solids and Surfaces Raveau, Bernard; Laboratoire de cristallographie et sciences des materiaux, Centre des Materiaux Supraconductors Al Rahal Al Orabi, Rabih; Central Michigan University Fornari, Marco; Central Michigan University, Physics Vaqueiro, Paz; University of Reading, Chemistry; Pasturel, Mathieu; Institut des Sciences Chimiques de Rennes, UMR CNRS 6226, Prestipino, Carmelo; Universite de Rennes 1, Institut Sciences Chimiques de Rennes - UMR 6226 Guilmeau, Emmanuel; Laboratoire de cristallographie et sciences des materiaux,

A tunable structural family with ultralow thermal conductivity: copper deficient $Cu_{1-x}\square_xPb_{1-x}Bi_{1+x}S_3$

Krishnendu Maji,[a] Pierric Lemoine,[b],* Adèle Renaud,[b] Bin Zhang,[c,d] Xiaoyuan Zhou,[c,d] Virginia Carnevali,[e] Christophe Candolfi,[f] Bernard Raveau,[a], Rabih Al Rahal Al Orabi,[e] Marco Fornari,[e],* Paz Vaqueiro,[g] Mathieu Pasturel,[b] Carmelo Prestipino,[b] Emmanuel Guilmeau[a],*

[a] CRISMAT, CNRS, Normandie Univ, ENSICAEN, UNICAEN, 14000 Caen, France

[b] Univ Rennes, CNRS, ISCR – UMR 6226, CNRS, F-35000 Rennes, France

[c] College of Physics and Institute of Advanced Interdisciplinary Studies, Chongqing University, Chongqing 401331, China

[d] Analytical and Testing Center of Chongqing University, Chongqing 401331, China

[e] Department of Physics and Science of Advanced Materials Program, Central Michigan University, Mt. Pleasant, MI 48859, USA

[f] Institut Jean Lamour, UMR 7198 CNRS – Université de Lorraine, 2 allée André Guinier-Campus ARTEM, BP 50840, 54011 Nancy Cedex, France

[g] Department of Chemistry, University of Reading, Whiteknights, Reading, RG6 6DX, United Kingdom

Abstract

Understanding the mechanism that connects heat transport with crystal structures and order/disorder phenomena is crucial to develop materials with ultra-low thermal conductivity (κ), for thermoelectric and thermal barriers applications and requires the study of highly pure materials. We synthesized the *n*-type sulfide $CuPbBi_5S_9$ with ultra-low κ of 0.4-0.6 W m^{-1} K^{-1} in the temperature range 300-700 K. In contrast to prior studies, we show that this synthetic sulfide does not exhibit the ordered gladite mineral structure but instead forms a copper-deficient disordered aikinite structure with partial Pb replacement with Bi, according to the chemical formula $Cu_{1/3}\square_{2/3}Pb_{1/3}Bi_{5/3}S_3$. By combining experiments and lattice dynamics calculations, we elucidated that the ultra-low κ of this compound is due to very low energy optical modes associated with Pb and Bi ions and, to a smaller extent, Cu. This vibrational complexity at low energy hints to substantial anharmonic effects that contributes to enhance phonon scattering. Importantly, we show that this aikinite sulfide, despite being a poor semiconductor, is a potential matrix for designing novel efficient *n*-type thermoelectric compounds with ultralow κ. A drastic improvement of the carrier concentration and thermoelectric figure of merit have been obtained upon Cl for S and Bi for Pb substitution. The $Cu_{1-x}\square_xPb_{1-x}Bi_{1+x}S_3$ series provides a new interesting structural prototype for engineering *n*-type thermoelectric sulfides by controlling disorder and optimizing doping.

1. Introduction

Energy scarcity and environmental concerns for a sustainable energy supply have been dramatically increasing over the last decades. In this context, power generation and waste heat recovery using thermoelectric (TE) materials [1–3] has become an important research endeavor. Thermoelectric devices require legs with *p*-type and *n*-type electrical carriers which are connected electrically in series and thermally in parallel and must satisfy strict demands in

terms of economic and environmental factors, thermo-mechanical stability, and energy conversion efficiency. Due to the low cost, non-toxicity, and high abundance of the precursors, synthetic sulfides have been the object of numerous investigations.[4–7] There are many *p*-type copper-rich sulfides[8-20] with values for the dimensionless thermoelectric figure of merit $ZT = S^2T/\rho\kappa$ (S, ρ, κ, and T represent the Seebeck coefficient or thermopower, electrical resistivity, total thermal conductivity, and operating temperature, respectively) up to $ZT \sim 1$ around 700 K. In contrast, very few *n*-type thermoelectric sulfides with *ZT* larger than 0.5 have been reported to date. These are represented by several binary, ternary and quaternary sulfides with moderate efficiency such as TiS_2 (*ZT* = 0.5 at 700 K),[21,22] $CuFeS_2$ (*ZT* = 0.21 at 573 K),[23] $CuFe_2S_3$ (*ZT* = 0.17 at 700 K),[24] CoSbS (*ZT* = 0.62 at 730 K),[25] $Cu_4Sn_7S_{16}$ (*ZT* = 0.21 at 600 K),[26–28] or thiospinel $Cu_2CoTi_3S_8$ (*ZT* = 0.2 at 670 K).[29,30] Recent studies on bismuth-based sulfides, however, have revealed promising families of *n*-type thermoelectrics with high *ZT* values. The performances of these materials stem in most cases from low thermal conductivity, which is thought to be due to the $6s^2$ bismuth lone pair of electrons[31] or to rattling mechanisms.[32] Their low thermal conductivity compensates for the moderate power factor ($S^2\sigma$) found for these materials. A typical example is the binary sulfide Bi_2S_3 which exhibits a maximum *ZT* of 0.6 at 773 K after Cl-doping.[33] Among the ternary Bi-sulfides, ultralow thermal conductivity was observed for cubic $AgBiS_2$ ($ZT \sim 0.2$ at 820 K).[34] Tan *et al.* recently reported *ZT* = 1 at 800 K in Cl-doped $AgBi_3S_5$.[35] This exceptional result was explained by invoking the complex crystal structure and the unusual 'double rattling' behavior associated with Ag and Bi atoms, leading to ultra-low thermal conductivity. Similarly, a new phase in the Cu-Bi-S ternary system, $Cu_{1.6}Bi_{4.8}S_8$, showed ultra-low thermal conductivity due to Cu rattling and *ZT* value of 0.26 at 736 K.[36] Two more *n*-type transition metal-based sulfides $MnBi_4S_7$ and $FeBi_4S_7$ with a layered structure built up of [MS_6] octahedra (M = Mn, Fe), BiS_6 octahedra, and distorted rectangular pyramids [BiS_5] were also

shown to exhibit moderate *ZT* values of 0.2 and 0.18 at 700 K, respectively.[37,38] A promising figure of merit *ZT* ~ 0.42 at 723 K was reported by Liang *et al.* for the gladite-type sulfide $CuPbBi_5S_9$.[39] The authors measured low thermal conductivity and moderate power factor, indicating that this phase is a potential *n*-type thermoelectric candidate. However, the synthesis did not lead to pure pristine samples and BiS_2 and metallic Bi secondary phases hindered the interpretation of the intrinsic transport properties of this material. It was suggested that the electron transport properties were significantly improved by the presence of Bi nanoparticles, while both the existence of pores and interfaces between the matrix and Bi particles were invoked as being responsible for the reduction in the lattice thermal conductivity. This justification, based on the interplay between several effects, is not conducive to clarify the relationship between the gladite structure and its thermoelectric properties and to derive strategies to improve the energy conversion performance; such a goal can be achieved, however, by investigating a highly pure Cu-Bi-S phase. Bearing in mind that $CuPbBi_5S_9$ corresponds to the member $x = 2/3$ of a large series of copper-deficient $Cu_{1-x}\square_xPb_{1-x}Bi_{1+x}S_3$ minerals,[40–46] we have revisited the crystal chemistry of this composition, using mechanical alloying and spark plasma sintering (SPS). In contrast to the results of Liang *et al.*,[39] we show that the synthetic sulfide with $x = 2/3$ ($CuPbBi_5S_9$) is highly pure and does not exhibit the ordered gladite mineral structure,[47,48] but instead a copper-deficient, partially disordered aikinite structure with Bi replacing Pb according to the chemical formula $Cu_{1/3}\square_{2/3}Pb_{1/3}Bi_{5/3}S_3$. Although the charge-balance $Cu^+\square_2Pb^{2+}Bi^{3+}{}_5S_9$ results in electronic properties characteristic of intrinsic semiconductors, we further demonstrate that this series provides an interesting platform to design novel *n*-type sulfides with ultralow thermal conductivity. Indeed, doping this sulfide with an excess bismuth or with chlorine on the Pb or S sites, respectively, enabled to significantly enhance the *ZT* values up to 0.43 at 700 K. This study

paves the way for the systematic investigation of a large series of *n*-type dopable thermoelectric sulfides.

2. Results and discussion

2.1. Structural and microstructural considerations

The quaternary Cu-Pb-Bi-S system contains a large number of minerals that are structurally related to aikinite $CuPbBiS_3$[40–42] and bismuthinite Bi_2S_3[43,44] (space group $Pnma$ with $a \sim a_a \sim 11.5$ Å, $b \sim b_a \sim 4$ Å and $c \sim c_a \sim 11.3$ Å). These phases can be formulated as $(Cu_{1-x}\square_x)Pb_{1-x}Bi_{1+x}S_3$, where □ refers to vacancies on the cationic sublattice of aikinite $CuPbBiS_3$. They crystallize either in the (normalized) space group $Pnma$ with $a \sim a_a$, $b \sim b_a$ and $c \sim n \times c_a$, or in the space group $Pmc2_1$ with $a \sim b_a$, $b \sim n \times c_a$ and $c \sim a_a$, n being a positive integer number. The ordered phases arising from the aikinite series can be constructed by substituting one Pb^{2+} plus one Cu^+ by one Bi^{3+} plus one vacancy; using two vacancies on three Cu sites as in gladite, we obtain:

$$3(CuPbBiS_3) \rightarrow 2\square'_{Cu} + Cu^{X}_{Cu} + Pb^{X}_{Pb} + 2Bi^{\bullet}_{Pb} + 3Bi^{X}_{Bi} + 9S^{X}_{S} + 2h^{\bullet} + 2e'.$$

The descriptions of these structures are based on three types of ribbons, which are arranged in a herringbone pattern.[45,46] A summary of the structural information of the ordered Cu-Pb-Bi-S phases arising from the aikinite – bismuthinite $(Cu_{1-x}\square_x)Pb_{1-x}Bi_{1+x}S_3$ series is presented in **Table 1**. In addition to these fully ordered $(Cu_{1-x}\square_x)Pb_{1-x}Bi_{1+x}S_3$ phases, some others were reported with mixed occupancy of some crystallographic sites and/or partial site occupancy, such as emilite $Cu_{10.7}Pb_{10.7}Bi_{21.3}S_{48}$ ($x = 0.33$, $Pmc2_1$, $n = 4$),[49] $Cu_{1.63}Pb_{1.63}Bi_{6.37}S_{12}$ ($x = 0.60$, $Pnma$, $n = 3$),[50] or $Cu_{1.435}Pb_{1.5}Bi_{6.5}S_{12}$ ($x = 0.60$, $Pmc2_1$, $n = 4$).[51] From a diffraction point of view, the long-range ordering of cations and vacancies leads to the presence of superstructure

diffraction peaks on powder diffraction patterns and superstructure spots in the selected area electron diffraction (SAED) patterns.

Table 1. Main structural information about ordered Cu-Pb-Bi-S phases arising from the aikinite – bismuthinite $(Cu_{1-x}\square_x)Pb_{1-x}Bi_{1+x}S_3$ series.

x	Chemical composition	Mineral name	Space group	n	Structure	Ref.
0.00	$CuPbBiS_3$	Aikinite	$Pnma$	1	2A	40–42
0.17	$Cu_5Pb_5Bi_7S_{18}$	Friedrichite	$Pmc2_1$	3	4A + 2K	52
0.33	$Cu_2Pb_2Bi_4S_9$	Hammarite	$Pnma$	3	2A + 4K	53
0.40	$Cu_3Pb_3Bi_7S_{15}$	Lindströmite	$Pnma$	5	2A + 8K	54,55
0.50	$CuPbBi_3S_6$	Krupkaite	$Pmc2_1$	1	2K	47
0.60	$Cu_{1.6}Pb_{1.6}Bi_{6.4}S_{12}$	Paarite	$Pnma$	5	8K + 2B	56
0.67	$CuPbBi_5S_9$	Gladite	$Pnma$	3	4K + 2B	47,48
0.83	$CuPbBi_{11}S_{18}$	Pekoite	$Pmc2_1$	3	2K + 4B	42
1.00	Bi_2S_3	Bismuthinite	$Pnma$	1	2B	43,44,57

When Pb and Bi on the one hand, and Cu and vacancies on the other hand, are disordered, the crystal structure can be described in the space group $Pnma$ with $a \sim a_a$, $b \sim b_a$ and $c \sim c_a$ as for aikinite. In that case, only minor changes in the intensity of the peaks associated with the aikinite structure are observed in non-resonant X-ray diffraction patterns. Indeed, from an X-ray diffraction point of view, these phases differ only by the Cu/vacancies content since Pb^{2+} and Bi^{3+} cations are isoelectronic. Consequently, their accurate identification remains difficult even with high-quality powder diffraction patterns. Note that an alternative to the above-mentioned individual superstructures (**Table 1**) was proposed by Petříček and Makovicky with the refinement of krupkaite $Cu_2Pb_2Bi_6S_{12}$, paarite $Cu_{1.7}Pb_{1.7}Bi_{6.3}S_{12}$, salzburgite $Cu_{1.6}Pb_{1.6}Bi_{6.4}S_{12}$ and gladite $Cu_{1.33}Pb_{1.33}Bi_{6.67}S_{12}$ phases as commensurately modulated structures by using the superspace group $Pmcn(0\beta0)00s$, where β was assumed to be 2, 1/5, 1/4 and 1/3, respectively.[46]

Synchrotron X-ray powder diffraction (XRPD) pattern recorded at room temperature (RT) on the pristine $CuPbBi_5S_9$ sample (after SPS) were indexed with an orthorhombic unit cell of the *Pnma* space group and parameters a = 11.4420(1) Å, b = 4.0187(1) Å and c = 11.2271(1) Å (**Figure 1**). The high purity of the sample is confirmed by the absence of extra diffraction

peaks as well as the good quality of the Rietveld refinement. Despite its chemical composition, which corresponds to gladite (**Table 1**), the absence of superstructure diffraction peaks (*i.e.* c ~11.2 Å instead of ~33.5 Å) suggests that the crystal structure of this $CuPbBi_5S_9$ sample can be described by considering disorder between Cu atoms and vacancies. A Rietveld refinement of synchrotron XRPD data was performed by considering an aikinite structural model (**Table 2**) with a 1/3 occupation of the Cu site according to the nominal composition. The differences between the two structural models are shown in **Figure 2**. Finally, as previously mentioned, Pb^{2+} and Bi^{3+} cannot be distinguished from non-resonant X-ray diffraction only. Consequently, the final Rietveld refinement was performed by considering the structural model reported by Mumme and Watts (**Figure 1** and **Table 2**).[42] Our synthetic $CuPbBi_5S_9$ can be described as a copper deficient aikinite $(Cu_{1/3}\square_{2/3})Pb_{1/3}Bi_{5/3}S_3$ with complete disorder between Cu^+ and vacancies on the copper site on the one hand and between $Pb^{2+}$and Bi^{3+} on the Pb site on the other hand. Note that an exchange of the cations between the initial Pb and Bi aikinite sites cannot be ruled out.

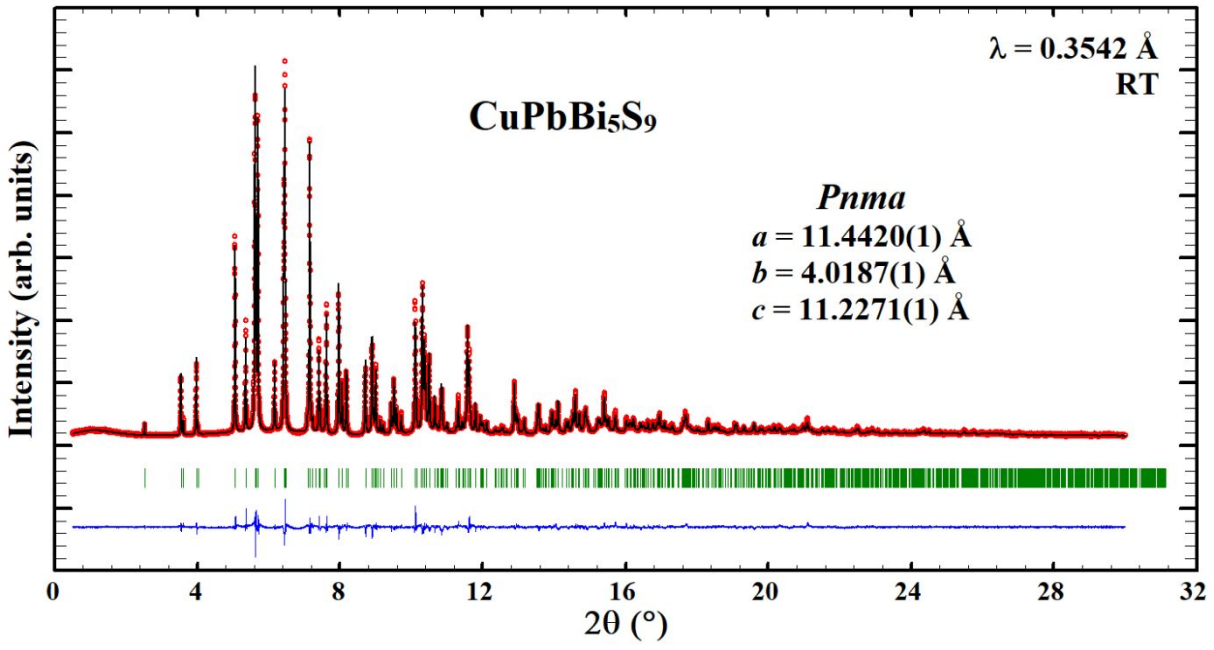

Figure 1. Rietveld refinement of the synchrotron XRPD data recorded at RT for spark plasma sintered pristine $CuPbBi_5S_9$ sample (λ = 0.3542 Å).

Table 2. Refined cell parameters and atomic coordinates of spark plasma sintered pristine $CuPbBi_5S_9$ (*Pnma*) from RT synchrotron XRPD data.

Atom	Site	x	y	z	Biso	SOF
Cu1	4*c*	0.2315(5)	1/4	0.2106(6)	4.23(20)	0.33
Pb2	4*c*	0.3377(1)	1/4	0.4739(1)	3.15(3)	0.33
Bi2	4*c*	0.3377(1)	1/4	0.4739(1)	3.15(3)	0.67
Bi3	4*c*	0.0167(1)	1/4	0.6772(1)	1.84(2)	1.00
S1	4*c*	0.0471(4)	1/4	0.1309(4)	3.14(13)	1.00
S2	4*c*	0.3784(4)	1/4	0.0571(4)	2.62(12)	1.00
S3	4*c*	0.2151(3)	1/4	0.8037(4)	1.52(10)	1.00
a = 11.4420(1) Å, b = 4.0187(1) Å, c = 11.2271(1) Å						
R_{Bragg} = 4.01, R_F = 3.92, R_{wp} = 4.57, R_{exp} = 2.22, χ^2 = 4.24						

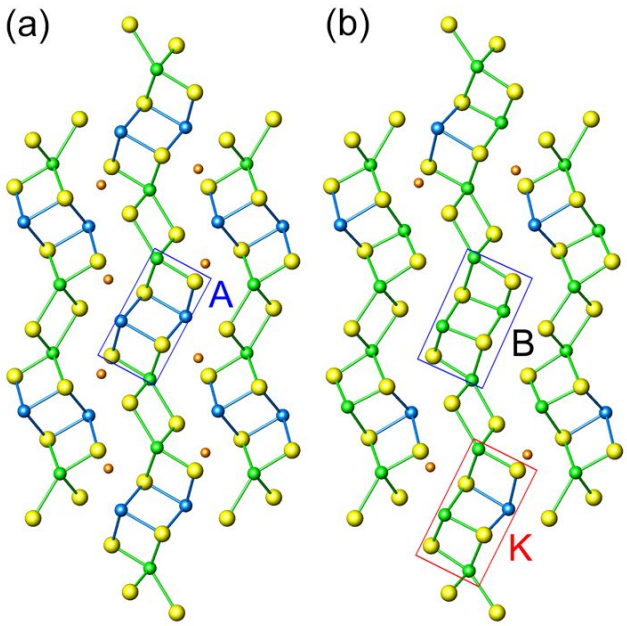

Figure 2. Comparison between the crystal structure of (a) aikinite and (b) gladite, with the aikinite-like (A), bismuthinite-like (B) and krupkaite-like (K) ribbons highlighted. Key: copper, orange spheres; bismuth, green spheres; lead, blue spheres; sulphur, yellow spheres.

Rietveld refinements of the XRPD data also confirms the Cu/vacancies disordered crystal structure and the high purity of the $CuPbBi_5S_{9-z}Cl_z$ samples with z = 0.03 and z = 0.09 (**Figures S1** and **S2**) and $CuPb_{1-y}Bi_{5+y}S_9$ sample with y = 0.05 (**Figure S3**). For the same reason that Pb^{2+} and Bi^{3+} are undistinguishable by non-resonant XRPD, S^{2-} and Cl^- cannot be as well distinguished. The Rietveld refinements of the Cl-doped samples were then conducted by considering the same structural model as the one used for pristine sample, *i.e.* only S^{2-} ions are considered in the structural model. These refinements show that Cl for S substitution does not significantly modify the crystal structure of the Cu-deficient aikinite $CuPbBi_5S_9$ (**Table**

3). The presence of extra diffraction peaks in the $CuPbBi_5S_{9-z}Cl_z$ sample with $z = 0.18$ (**Figure S4**) and $CuPb_{1-y}Bi_{5+y}S_9$ samples with $y = 0.10$, 0.25 and 0.50 (**Figure S5 and S6**) is related to the presence of a secondary phase in the Cu-(Bi,Pb)-S system. However, due to the almost identical atomic number of Bi and Pb, the exact nature and composition of this phase have not been identified. This indicates that Cl for S and Bi for Pb substitutions may be limited due to the key role of the (Cu+Pb)/Bi ratio to stabilize the structure.

Table 3. Refined unit cell parameters and reliability factors of the pristine and $CuPb_{1-y}Bi_{5+y}S_{9-z}Cl_z$ samples from the Rietveld analysis of the room temperature XRPD data and corresponding reliability factors.

Compound	$CuPbBi_5S_9$	$CuPbBi_5S_{8.97}Cl_{0.03}$	$CuPbBi_5S_{8.91}Cl_{0.09}$	$CuPb_{0.95}Bi_{5.05}S_9$
Space group	*Pnma*	*Pnma*	*Pnma*	*Pnma*
a (Å)	11.4342(2)	11.4301(3)	11.4345(2)	11.4301(3)
b (Å)	4.0152(1)	4.0138(1)	4.0131(1)	4.0111(1)
c (Å)	11.2191(2)	11.2108(3)	11.2067(2)	11.2079(3)
V (Å^3)	515.08(2)	514.33(3)	514.26(2)	513.85(2)
R_{Bragg}, R_F	4.73, 3.30	4.44, 2.96	5.41, 3.70	4.79, 3.50
R_{wp}, R_{exp}	7.25, 4.85	5.70, 4.10	6.26, 4.20	8.73, 7.47
χ^2	2.24	1.94	2.22	1.37

To investigate the microstructure of $CuBiPb_5S_9$ sample, systematic transmission electron microscopy (TEM) studies were conducted. As shown in **Figures 3a and 3b**, the sample exhibits nano-grains with size of ~ 200 nm and irregular shapes. Numerous bubble-like cavities — shown as bright contrast in TEM images (**Figure 3a**) and dark contrast in high-angle annular dark-field images (HAADF, **Figure 3b**) — can be observed near the grain boundaries, especially at the trigeminal ones. Those cavities may be due to element diffusion (incomplete sintering) or volatilization at high temperature during sintering. The electron dispersion spectroscopy (EDS) mapping images (**Figure 3c**) demonstrate a uniform chemical distribution with the exception of minor Cu/Pb-rich precipitates. The cationic disorder of these samples is further confirmed by our TEM studies. Detailed comparison between ordered gladite and disordered phases are presented in **Figure S7**. Tilting series were carried out for structure identification, during which SAED patterns and corresponding high-resolution TEM images were recorded (**Figure 3d and 3k**). The inserted Kikuchi patterns in **Figure 3d, 3f,**

and 3h support the orientation relationships between different SAED patterns. The fast Fourier transform patterns are also shown in the TEM images. A grain was continuously tilted to the [010] (**Figure 3d and 3e**), the [160] (**Figure 3f and 3g**) and the [140] (**Figure 3h and 3i**) zone axis, respectively. As expected, these SAED patterns are consistent with those of the disordered simulated patterns. Further tilting of the thin slice to the [071] zone (**Figure 3j and 3k**), made the ordered and disordered configurations almost indistinguishable (**Figure S7d**). Furthermore, similar microstructure and disorder were found in $CuPb_{0.95}Bi_{5.05}S_9$ and $CuPbBi_5S_{8.91}Cl_{0.09}$ samples (**Figure S8 and S9**, respectively).

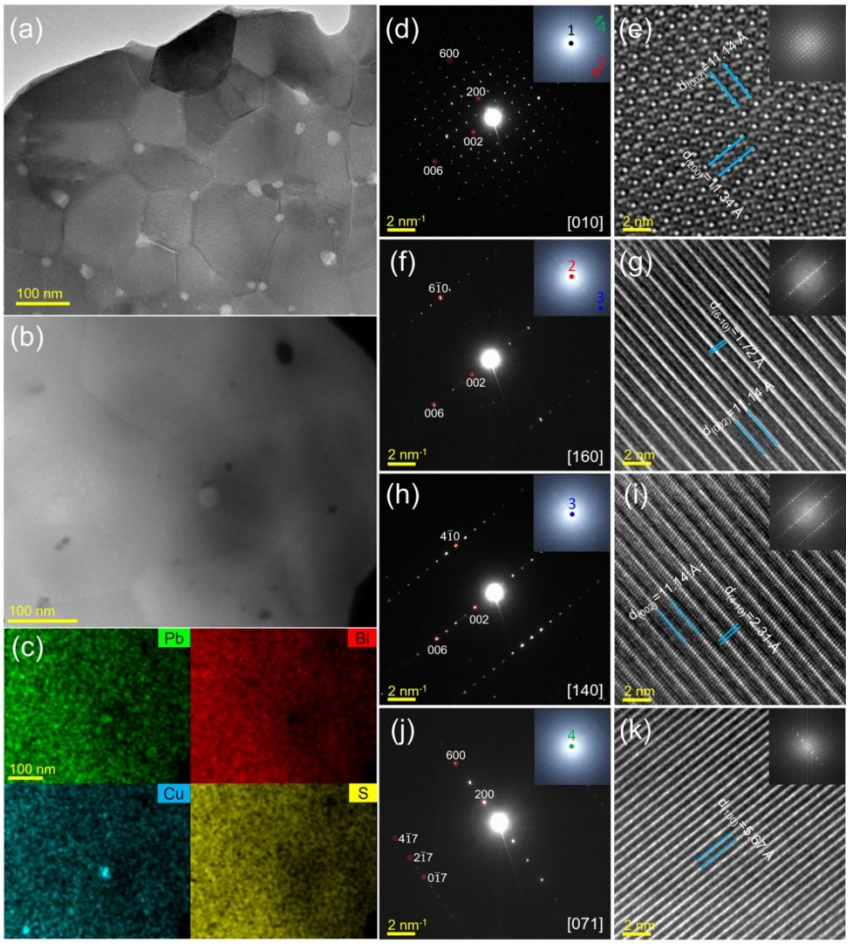

Figure 3. Structure analysis of $CuBiPb_5S_9$ sample by TEM. (a) low-mag TEM image, (b) HAADF image and (c) the corresponding EDS mappings of Pb, Bi, Cu, S, respectively, (d-k) SAED patterns (Kikuchi patterns as inset) and the related HRTEM images (inset: FFT patterns) along selected zone axes. Bubble-like cavities appear as opposite contrast with white and dark in (a) TEM and (b) STEM-HAADF images, respectively, due to different imaging modes.

Micrographs, taken by scanning electron microscopy (SEM) on the polished (**Figure S10**) and fractured (**Figure S11**) surfaces, confirm the high purity of the pristine sample and the fine microstructure. The very small grain size, as observed by TEM to be around 200-300 nm, is induced by the combined mechanical alloying and SPS processes. Backscattered electron imaging (BSE) combined with EDX analysis (**Figure S11**) confirms the homogeneous distribution of all elements for the pristine sample and highlights the presence of bubble-like cavities already observed by TEM, probably occurring from incomplete sintering or sulfur volatilization during the SPS process. For Cl- and Bi-doped series, small grain sizes are also observed for all the samples. With increasing Cl and Bi contents, the presence of Cu-Bi-S impurity phases (dark contrast) could be detected (**Figure S10**) in the Cl-doped (z = 0.18) and Bi-doped (y = 0.25 and 0.50) samples.

Note that the formation energies for aikinite, ordered gladite, and several models for copper deficient aikinite computed by first-principles total energy methods are all between -0.371 eV and -0.345 eV, the lowest being aikinite. These results indicate the possibility of coexisting configurations. Total energy calculations indicate a very small interaction between Cu-vacancies and Bi on Pb-sites (**Figure S12**).

2.2. Electronic structure

First-principles density functional theory (DFT) calculations were used to complement the experimental data. We studied the fully ordered gladite and several disordered models which have different level of disorder: a combination of vacancies on the Cu site, Bi on the Pb site, and Cl-S substitutions. The formation energy surface is reasonably flat ($\Delta E \leq 13$ meV/atom). From the electronic structure perspective, pristine gladite is an intrinsic semiconductor/insulator with a forbidden energy gap of 0.92 eV (**Figure 4**, see Section 4 for computational details. Note that the band-structure is meaningful only for ordered gladite. The

computed value is in agreement with the band gap determined from Kubelka-Munk transform which provides values ranging from 0.89 to 0.95 eV, assuming direct transitions (see next paragraph). As expected, the valence manifold is mainly formed by Cu and S states while the conduction band has a larger Bi and Pb contribution. From a purely theoretical point of view, the top of the valence band could provide holes with large effective masses (**Figure S13**).

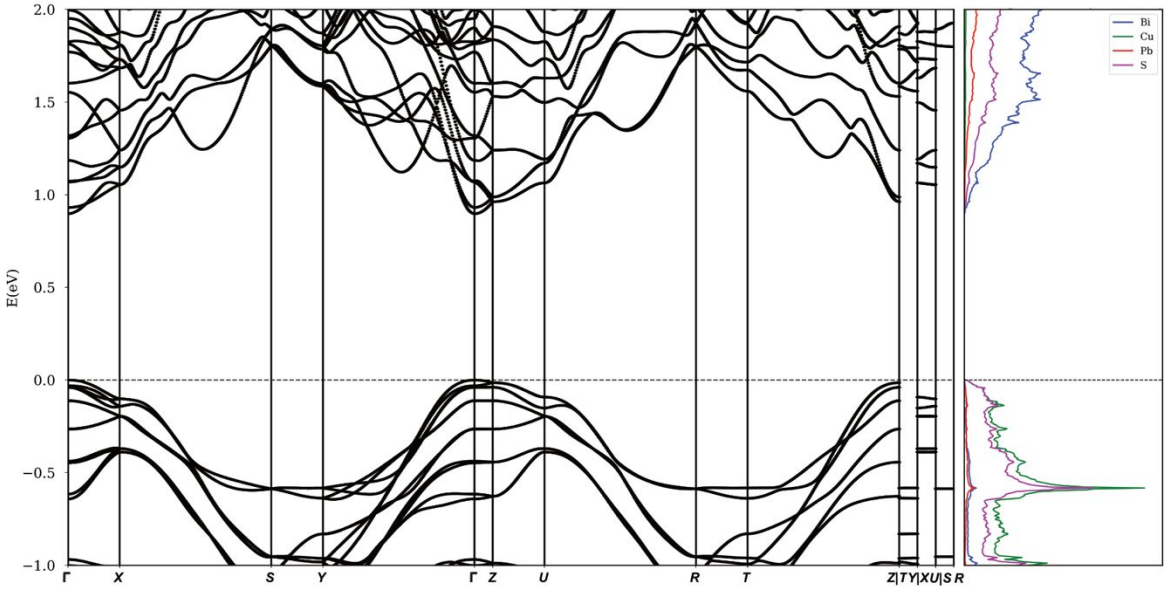

Figure 4. Electronic band structure (left) and projected electronic density of states (right) of ordered $CuPbBi_5S_9$ computed within the ACBN0 approach with U(Pb) = 0.005, U(Cu) = 1.269, U(Bi) = 0.043, and U(S) = 2.774. The horizontal line indicates the zero-energy reference that we arbitrarily set to the top of the valence band. The Fermi level is not drawn and always sits near the middle of the band gap for an intrinsic semiconductor.

In proximity of the forbidden energy gap, the electronic properties are of course sensitive to the effect of disorder as well as chemical replacements. **Figure 5** shows the electronic density of states (eDoS) for gladite and several models of Cu-deficient disordered aikinite; we have averaged the different contributions to reasonably represent the eDoS of the macroscopic sample. eDoS, Seebeck coefficient, and electrical resistivity are also greatly affected by the specific supercell used to model the disordered configurations (**Figure S13 and S14**) making it difficult to reconcile a microscopic theoretical perspective with experiments. Transport

calculations within the constant scattering time approximation are limited in the presence of substantial disorder.

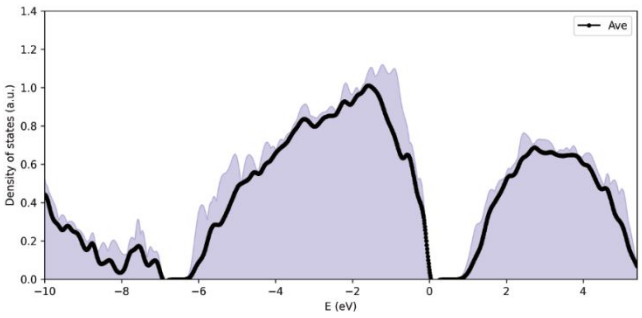

Figure 5. Average eDoS on the several computational cells used to model the ordered gladite as well as vacancies and Pb-Bi disordered system. The average gap between valence and conduction bands is of the order of 0.9 eV.

The gladite structure includes a chain of Bi atoms in the proximity of Cu vacancies. The electron localization function (ELF) and the charge density isosurfaces (**Figure 6)** clearly points to the presence of a lone-pair near Bi and charge rearrangements near S atoms surrounding the vacancies.

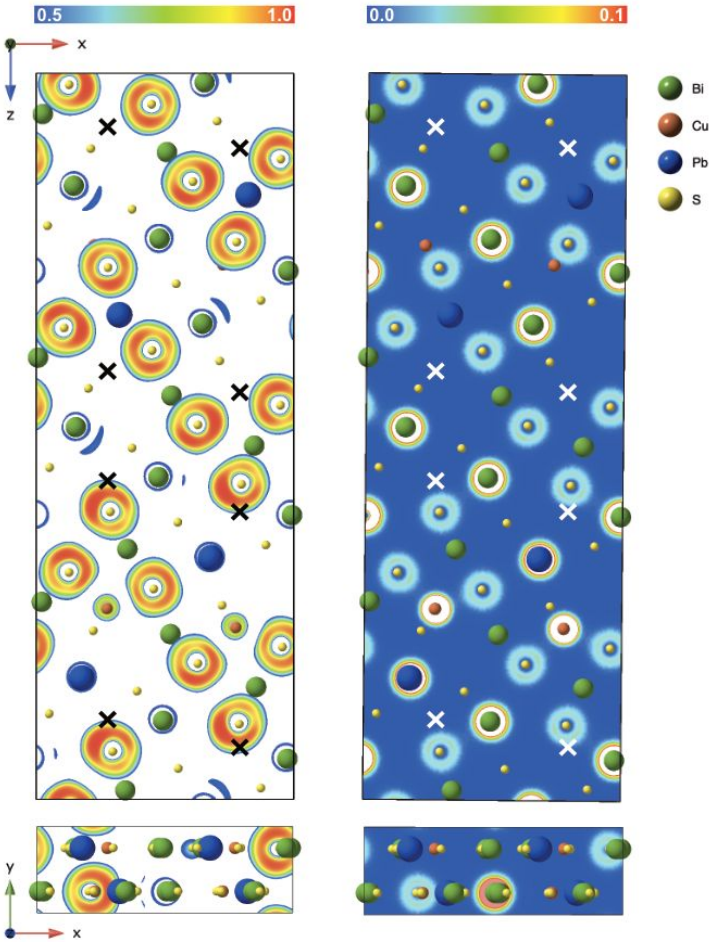

Figure 6. Side (top panel) and top (bottom panel) view of the contour of the electron localization function (left) and charge density (right) of ordered $CuPbBi_5S_9$. Values for the ELF range between 0 and 1: ELF = 0.5 (blue contours) indicates free-electron behavior and ELF = 1.0 (red contour) indicates strong localization. Values smaller than 0.5 are not easily interpretable. Values for the charge density range between 0.0 (blue) and 0.1 (red). Black and white crosses indicate the positions for the Cu vacancies in the ELF and charge density plots respectively.

Band gaps, determined from Kubelka-Munk transforms (**Figure 7a)**, indicate that the substitution of chlorine for sulfur tends to slightly open the band gap from 0.89 eV for $CuPbBi_5S_9$ to 0.95 eV for $CuPbBi_5S_{8.82}Cl_{0.18}$, assuming direct transitions. A similar conclusion is drawn by considering indirect transitions (**Figure S15**). This behaviour may be explained by the differences in anionic radii and electronegativity of S and Cl. We note that all the samples seem to remain non-degenerate, suggesting that the Burnstein-Moss effect[58,59] observed in heavily-doped semiconductors that leads to an increasing energy band gap with doping level has probably little influence in the present case. By combining electrochemical

and optical measurements, energy levels in an absolute energy scale with respect to the vacuum level were also estimated (see details in experimental section and **Figures S16 and S17**). Cl-doping affects the localization of the Fermi level, as the flat band potential values extrapolated at $C^{-2} = 0$ from the Mott-Schottky plots (**Figure 7b**) exhibit a slight shift towards lower energy of the Fermi level, suggesting a complex interplay between Cl-doping, S-vacancies, and possibly other defects.

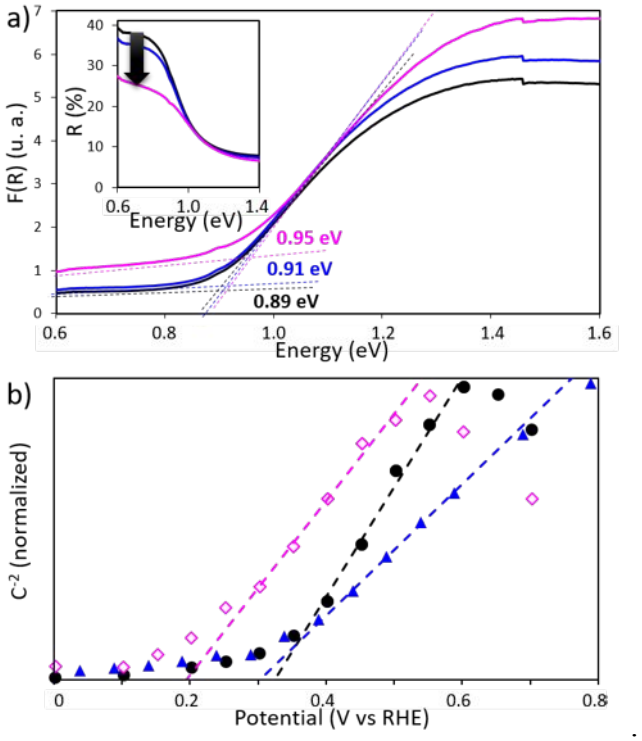

Figure 7. a) Kubelka-Munk transforms, and b) Mott-Schottky plots for $CuPbBi_5S_9$ (black, ●), $CuPbBi_5S_{8.91}Cl_{0.09}$ (blue, ▲) and $CuPbBi_5S_{8.82}Cl_{0.18}$ (pink, ◊) samples.

2.3. Electronic transport properties

The electrical properties in the $CuPbBi_5S_{9-z}Cl_z$ series (z = 0.00, 0.03, 0.09, 0.18) over the temperature range 300 - 700 K are displayed in **Figure 8**. The undoped pristine $CuPbBi_5S_9$ is highly resistive (electrical resistivity $\rho = 3.5\times10^5$ Ω cm and $S = -1370$ μV K^{-1} at 375 K, **Figure 8a and 8b**). Both the electrical resistivity and absolute value of the Seebeck coefficient $|S|$ decrease with increasing temperature to 1.25 Ω cm and 600 μV K^{-1} at 700 K,

respectively, indicative of a non-degenerate semiconducting behavior. Negative values of the Seebeck coefficient are measured for all compositions over the entire temperature range, indicating that electrons are the dominant charge carriers. The *n*-type conduction is mainly due to sulfur vacancies similar to other systems like Bi_2S_3, $MnBi_4S_7$, $FeBi_4S_7$, $AgBi_3S_5$ etc.[33,35,37] In comparison to other Bi-S based compounds, pristine phase $CuPbBi_5S_9$ is quite resistive at RT. For example, pristine Bi_2S_3 has an electrical resistivity of 0.25 Ω cm at RT, whereas other well-known ternary compounds, like $AgBi_3S_5$ and $MnBi_4S_7$, have a RT electrical resistivity value of 0.24, 5.3×10^{-3} and 7.1×10^{5} Ω cm, respectively. The thermopower is also quite large in our compound and significantly higher than in other Bi-based sulfides. For instance, Bi_2S_3 and $AgBi_3S_5$ have $|S|$ values of 350 and 150 μV K^{-1} at RT, respectively. Those lower values are mainly explained by the larger carrier concentrations (respectively 3.7×10^{16} cm^{-3} and 4.1×10^{18} cm^{-3} for Bi_2S_3 and $AgBi_3S_5$) due to non-stoichiometric effects. Pristine $CuPbBi_5S_9$ sample exhibits a carrier concentration at RT around 4.5×10^{12} cm^{-3} which is exceptionally low and rare in polycrystalline chalcogenides. Such low carrier concentration, in agreement with the large Seebeck coefficient, suggests that our material is highly stoichiometric thanks to the synthesis process combining mechanical-alloying and SPS. As seen in other sulfides, the optimized mechanical alloying process combined with SPS densification favors the crystallization of stoichiometric compounds by preventing loss in quartz tubes exposed to high temperature and small temperature gradients inside a furnace.[17,26] Note that $|S|$ and ρ values of 950 μV K^{-1} and 7.1×10^{3} Ω cm at RT, respectively, were measured by Liang *et al.* on a $CuPbBi_5S_9$ sample prepared by mechanical alloying+SPS,[39] suggesting a significant stoichiometry deviation in their sample. Both $|S|$ and ρ values decrease gradually with the increase of Cl content, down to 350 μV/K and 0.41 Ω cm for $z = 0.09$ at 300 K. $|S|$ and ρ decrease monotonically with increasing temperature for all the compositions, which indicates that the materials behave as non-degenerate semiconductor

upon Cl-doping, although additional electron are injected in the matrix. The decrease of $|S|$ and ρ with increasing Cl content, however, is consistent with the role of chlorine as an electron donor as it replaces sulfur. With increasing Cl content, the carrier concentrations at room temperature increases up to 5.5×10^{16} for z = 0.03, 1.5×10^{18} for z = 0.09 and 1.9×10^{18} cm^{-3} for z = 0.18. The RT mobility (μ) values are equal to 3.7, 4.15, 7.0 and 2.5 $cm^2\ V^{-1}\ s^{-1}$ for z = 0, 0.03, 0.09, 0.18, respectively. Those values are significantly smaller than those measured in the other Bi-based compounds mentioned before, which is mainly explained by the very small grain size and/or the disordered structure in our samples. Further investigations are ongoing to determine the impact of the crystal structure and microstructure on the electron mobility.

Finally, it must be noted that the measurements are well reversible up to 680 K (3 cycles from 350 K to 630 K + 3 cycles from 350 K to 680 K) which attests the stability of our material in this working temperature range (**Figure S18**). A slight drift is observed with the addition of 3 more cycles up to 700 K. This phenomenon can be related to surface oxidation of the sample in the ZEM3 chamber and/or sulfur loss or phase decomposition. Interestingly, a hysteresis loop can be observed at around 370-520 K, which is most probably related to order/disorder phenomena. Different studies on related natural minerals, such as pekoite $CuPbBi_{11}S_{18}$, hammarite $CuPb_2Bi_4S_9$ and krupkaite $CuPbBi_3S_6$, have shown that the temperature limit to order vacancies is below 473-573 K.[42,45,60] When heating up our sample up to 448 K, the vacancies on the Cu site probably start to order, and then disorder above 473 K. This point is still under investigation.

The power factor (*PF*) as a function of temperature in the $CuPbBi_5S_{9-z}Cl_z$ series is shown in **Figure 8c**. The undoped sample exhibits a very low power factor of 0.22 μW $cm^{-1}\ K^{-2}$ at 700 K. The power factor increases significantly with Cl content to a maximum value of 2.2 μW $cm^{-1}\ K^{-2}$ at 700 K for z = 0.09. This value is slightly lower than the value of 2.9 μW $cm^{-1}\ K^{-2}$

reported by Liang *et al*.[39] In comparison to other systems, the *PF* values in $CuPbBi_5S_{9-z}Cl_z$ are comparable with those of $MnBi_4S_7$ and $FeBi_4S_7$ (~ 2.1 μW cm^{-1} K^{-2} at 550 K)[37], but remain lower than the best performing compounds, in particular, 0.5 mol% $BiCl_3$ doped Bi_2S_3 sample and 0.33% Cl doped $AgBi_3S_5$ samples, which exhibit very high *PF* values of 6.7 and 7.0 μW cm^{-1} K^{-2}, respectively.[33,35] The difference is mainly explained by intrinsic effects (crystal structure, electronic structure, defects) and extrinsic effects (grain size).

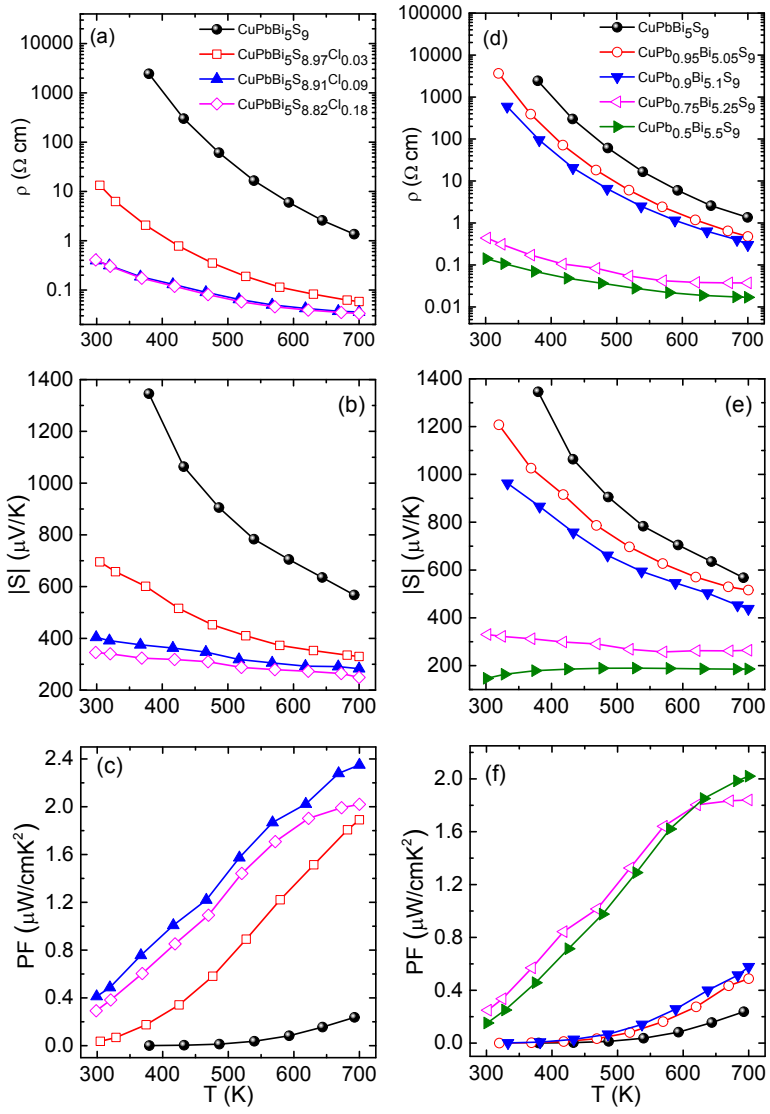

Figure 8. Temperature dependence of (a,d) electrical resistivity, (b,e) Seebeck coefficient and (c,f) power factor in the $CuPbBi_5S_{9-z}Cl_z$ and $CuPb_{1-y}Bi_{5+y}S_9$ series, respectively.

The electrical transport properties in the second $CuPb_{1-y}Bi_{5+y}S_9$ series are displayed in **Figure 8 (d,e,f)**. The electrical resistivity and absolute value of the Seebeck coefficient decrease as the Bi content increases. The lowest value of ρ of 0.14 Ω cm and $|S|$ of 144 μV K^{-1} at 300 K are obtained for $CuPb_{0.5}Bi_{5.5}S_9$. For this sample, the electrical resistivity slightly decreases with increasing temperature while $|S|$ increases. The carrier concentration in this series increases with Bi doping to 7.7×10^{13} cm^{-3} for y = 0.05, 4.6×10^{18} cm^{-3} for y = 0.25, and reaches a maximum of 1.9×10^{19} cm^{-3} for y = 0.5. Those values and trends must be, however, taken with caution as the material is composed of different phases for y = 0.25 and y = 0.5. The highest *PF* value of 0.24 μW cm^{-1} K^{-2} at RT is obtained for $CuPb_{0.75}Bi_{5.25}S_9$ (*PF* = 1.83 μW cm^{-1} K^{-2} at 700 K).

As expected, $|S|$ decreases with increasing the electron concentration n_H for both series. This general trend, illustrated by the Ioffe-Pisarenko plot shown in **Figure 9**, is well captured by a single-parabolic band (SPB) model with acoustic phonon scattering (see SI for equations) and a conduction density-of-states effective mass m^*_{DOS} of 0.88 m_e. This good agreement suggests that Cl or Bi doping weakly influences m^*_{DOS}, with no evident sign of multiband behavior at these doping levels.

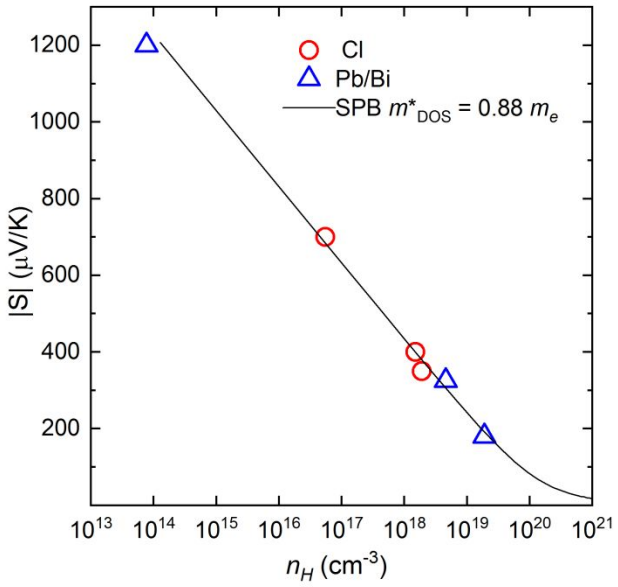

Figure 9. Ioffe-Pisarenko representation of the Seebeck coefficients $|S|$ as a function of the electron concentration n_H at 300 K. The solid black curve was calculated using a single-parabolic band approximation.

2.4. Thermal transport properties

As shown in **Figure 10**, the pristine phase exhibits a very low total thermal conductivity κ of 0.59 W m^{-1} K^{-1} at 300 K, which decreases upon warming to 0.47 W m^{-1} K^{-1} at 700 K. Both the magnitude and temperature dependence of κ are in agreement with the data reported by Liang *et al.* on pristine $CuPbBi_5S_9$.[39] The thermal conductivity only weakly varies with increasing Cl and Bi contents, with values ranging between 0.50 and 0.65 W m^{-1} K^{-1} at 300 K. Due to the relatively high electrical resistivity of the samples, the electronic contribution κ_e to κ is negligible making the lattice component κ_L the primary contribution. Interestingly, κ_L exhibits a weaker temperature dependence than the T^{-1} law expected for Umklapp scattering, with a decrease following $T^{-0.35}$ and $T^{-0.5}$ dependences for the Cl and Pb/Bi series, respectively. This deviation from the conventional law has been observed in several chain-like compounds such as TlSe, InTe, $TlInTe_2$, TlCuSe or Tl_3MX_4 (M = V, Nb and Ta; X = S and Se) and in tetrahedrites,[61-72] all of them showing ultralow κ_L at high temperatures. Theoretically, these

deviations have been shown to be a signature of strong intrinsic anharmonicity resulting in pronounced renormalization effects on the phonon frequencies of optical modes that shape the low-energy part of the phonon spectrum of these materials.[61–73] These similarities suggest that $CuPbBi_5S_9$ may also show an anharmonic behavior. At high temperatures, κ_L approaches the minimum lattice thermal conductivity κ_{min} of 0.26 W m^{-1} K^{-1}, calculated from the measured room-temperature longitudinal (v_l = 3074 m s^{-1}) and transverse (v_t = 1565 m s^{-1}) sound velocities according to the model of Cahill and Pohl,[74] indicating a near-minimum phonon mean free path. The lack of significant decrease upon varying the Cl and Bi contents indicates that the crystal structure is the dominant factor that limits the propagation of heat carriers. Of note, κ_L is significantly lower than those measured in binary and ternary sulfides such as Bi_2S_3, PbS, TiS_2, $MnBi_4S_7$,[22,33,37,75] and is comparable with those measured in several Bi-based sulfides such as $AgBiS_2$ and $AgBi_3S_5$.[34,35]

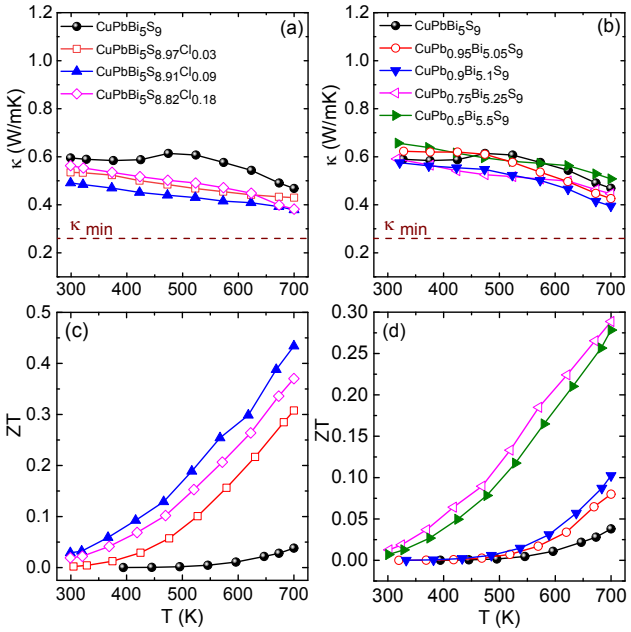

Figure 10. Temperature dependence of (*a,b*) thermal conductivity and (*c,d*) figure of merit *ZT* in the $CuPbBi_5S_{9-z}Cl_z$ and $CuPb_{1-y}Bi_{5+y}S_9$ series, respectively.

To further understand the origin of the very low κ_L values, insights into the lattice dynamics of $CuPbBi_5S_9$ have been obtained by low-temperature specific heat C_p measurements. The low-temperature data follow the conventional relation $C_p = \gamma T + \beta T^3$ where γT and βT^3 are the electronic and lattice contributions, respectively. The zero value of γ confirms the semiconducting ground state of $CuPbBi_5S_9$. The Debye temperature θ_D, inferred from the relation $\theta_D = (12\pi^4 nR/5\beta)^{1/3}$ where n is the number of atoms per formula unit and R is the ideal gas constant, is equal to 156.5 K. As observed in several families of sulfides such as tetrahedrites and colusites, and in cage-like materials,[36,66–70,76-78] the $C_p(T)$ data show a pronounced peak centered near 10 K upon plotting the $C_p(T)/T^3$ versus T. This plot shows that low-energy optical modes exist in the phonon spectrum. To model this peak, we used a combination of a Debye term with two additional Einstein-like terms (see SI for the equation and physical parameters) to account for the low-lying optical modes. In this model, the Debye temperature, the number of Debye and Einstein oscillators, and the characteristic Einstein temperatures are considered as free parameters. The best fits to the data, shown in **Figure S19**, yield Einstein temperatures θ_{E1} and θ_{E2} of 32 and 48.4 K with spectral weights of 0.40 and 0.33, respectively. According to atomic mass considerations, this excess contribution to C_p is mainly associated with low-energy optical modes from the Bi and Pb atoms. First-principles lattice dynamics calculations on aikinite confirm such a conjecture (**Figure 11**). Indeed, using aikinite as a proxy for the Cu-deficient disordered aikinite, the phonon dispersions indicate the presence of very low energy optical modes associated with Pb and Bi ions and, to a smaller extent, Cu. The Einstein temperatures inferred from the specific heat data, that correspond to wavenumbers of 22.2 and 33.6 cm^{-1}, respectively, are in good agreement with the two lowest peaks (25.0 and 35.2 cm^{-1}, respectively) observed in the PDOS mainly associated with Pb-weighed thermal motions. This vibrational complexity at low energy hints to possible substantial anharmonic effects that contribute to lower κ_L. This is in

agreement with the high value of the Grüneisen parameter γ of 1.93, obtained from the sound velocity measurement at 300 K (using Eq. S2). Such a large value, close to those reported for other ultralow-κ_L materials (**Table 4**), is consistent with strong phonon-phonon scattering in $CuPbBi_5S_9$. Similar characteristics have been observed in the phonon spectra of the above-mentioned chain-like and sulfide compounds, all of them exhibiting ultralow κ_L.[79–83] The presence of soft bonding interaction in $CuPbBi_5S_9$ is further supported by the low average sound velocity v_s of 1758 m s^{-1} (see eq. S4), which is comparable with published data[39] on $CuPbBi_5S_9$ and with other low-thermal-conductivity chalcogenides (**Table 4**).

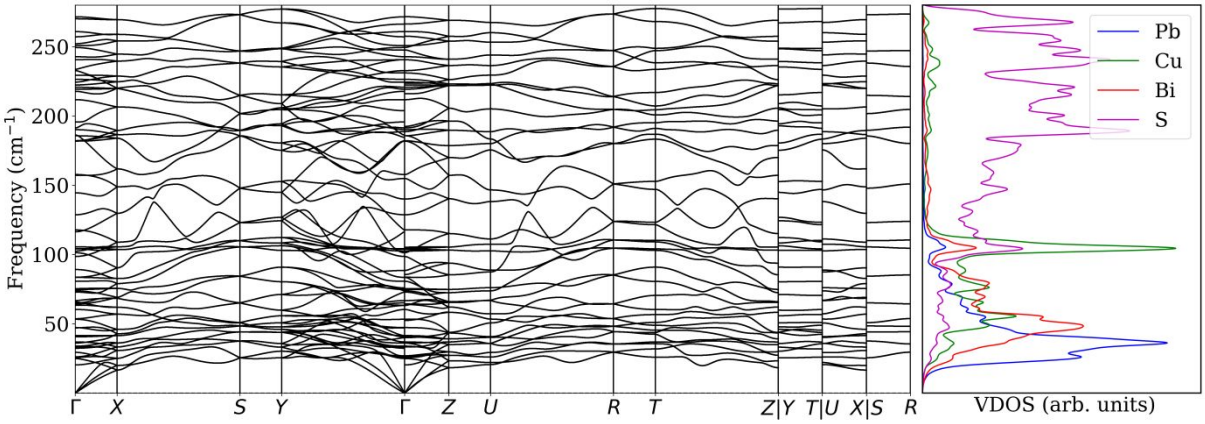

Figure 11. Phonon dispersions (left) and projected phonon density of states (PDOS) (right) of aikinite $CuPbBiS_3$ which we used as proxy for the Cu-deficient disordered aikinite. The low-frequency optical vibrations are mainly associated with the heavier cations. The contribution of Cu in the low-frequency region of the spectrum is not negligible as it was recognized in other sulfides.

Table 4. Grüneisen parameter and Debye temperature from sound velocity measurements: comparison including Cu-deficient aikinite and several other sulfides.

Compound	Average sound velocity (m/sec)	Grüneisen parameter	Debye T (K)	Ref.
$CuPbBi_5S_9$	1758	1.93	178.5	This work
$MnBi_4S_7$	1767	1.16	179.4	37
$FeBi_4S_7$	1967	1.28	200.8	37
$AgSbTe_2$	1727	2.05	125	79
$BiSbSe_3$	1629	1.89	165	80
SnSe[81]	1420	3.13	142	81
Bi_2Se_3[82]	2083	1.65	205	82
Sb_2Se_3[80]	1882	1.58	180	80

The temperature dependence of *ZT* in the $CuPbBi_5S_{9-z}Cl_z$ and $CuPb_{1-y}Bi_{5+y}S_9$ series (**Figure 10c and 10d**, respectively) points to limited thermoelectric efficiency for pristine $CuPbBi_5S_9$ ($ZT = 0.04$ at 700 K). However, the figure of merit increases remarkably with Cl-doping reaching 0.43 for $z = 0.09$. A similar increase in *ZT* is also observed with increasing Bi content, reaching 0.29 for $y = 0.25$ sample (**Figure 10d**). Comparing the performance at 700 K with other Bi-based *n*-type thermoelectric sulfides (**Figure 12**), it is possible to qualitatively estimate the interplay between lattice thermal conductivity and power factors on *ZT*. Cl-doped $CuPbBi_5S_9$ exhibits similar *ZT* compared to Cl-doped Bi_2S_3 compound, one of best *n*-type state-of-the-art thermoelectric sulfides. $CuPbBi_5S_9$ presents a significantly lower lattice thermal conductivity compared to this material thanks to its structural complexity and enhanced structural disorder. However, this is counterbalanced by a lower power factor (2.2 $\mu W\ cm^{-1}\ K^{-2}$ compared to 6.0 $\mu W\ cm^{-1}\ K^{-2}$) due to a carrier concentration one order of magnitude larger in Cl-doped Bi_2S_3. The absence of cationic disorder in the latter compound also favors a higher electron mobility. The very large *ZT* in $AgBi_3S_5$ mainly originates from a larger carrier concentration, at least 15 times higher than in our compounds, due to a higher concentration of defects, while presenting similar lattice thermal conductivity. This suggests that a drastic improvement of *ZT* can be achieved in $CuPbBi_5S_9$ and in the large family of $Cu_{1-x}\square_xPb_{1-x}Bi_{1+x}S_3$ compounds provided that a higher carrier concentration can be reached. To estimate the maximum *ZT* value achievable upon doping in $CuPbBi_5S_9$, the dimensionless quality factor *B* has been calculated for the $z = 0.09$ sample (see SI for the equations). This parameter, which encompasses all the inherent material properties that determines the *ZT* values,[84–86] enables to calculate the dependence of the *ZT* values on the reduced chemical potential η, that is, on the doping level. Using the *S* and κ_L values of the $z = 0.09$ sample measured at 700 K yield a *B* value of ~ 0.3 that corresponds to a maximum *ZT* of 0.8 reached at an optimum *S* value of ~ 200 $\mu V\ K^{-1}$. This last value, which fits well with the range of

optimum *S* values predicted in several studies,[85,87,88] shows that the carrier concentration should be further increased using other aliovalent substitutions.

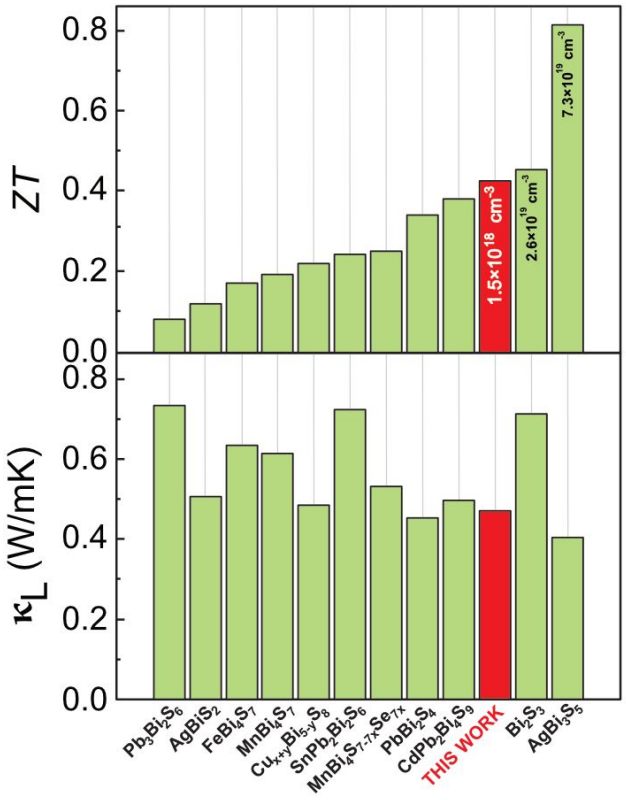

Figure 12. (Top panel) *ZT* and (bottom panel) lattice thermal conductivity in state-of-the-art thermoelectric *n*-type Bi-based sulphides.[33–35,37,38,83,89–91] The values inside the histogram bars are the carrier concentration.

3. Conclusion

A new Cu-deficient aikinite-type sulfide has been synthesized with the $CuPbBi_5S_9$ composition by combining mechanical alloying and SPS techniques. The structure of this sulfide, though closely related to gladite with the same composition reported by Liang *et al.*[39], differs from the latter by the disordered distribution of copper and vacancies on the cationic sites. In contrast to their $CuPbBi_5S_9$ compound, which could only be obtained with the presence of secondary phases, this Cu-deficient aikinite is highly pure allowing for a detailed investigation of its transport properties. In particular, we have demonstrated that the ultralow lattice thermal conductivity observed for this structural type is intrinsic and does not originate

from secondary phases. Despite being a nearly intrinsic semiconductor (ρ ~5.10^3 Ω cm and S ~ -1300 μV K^{-1} at 400K) with extremely low carrier concentration (4.5×10^{12} cm^{-3}), this synthetic sulfide is an exceptional prototype for generating high thermoelectric performance by doping with Cl or Bi, leading to thermoelectric figures of merit varying between 0.30 and 0.43 at 700 K. The good thermoelectric performance stems from the exceptionally low lattice thermal conductivity due to the presence of very low energy vibrations involving Bi, Pb, and Cu. The dramatic improvement of the thermoelectric figure of merit upon Cl- or Bi-doping may be related to the ability of the Bi-S framework to generate *n*-type conductivity due to the so induced Bi^{3+}/Bi^{2+} mixed valence. This statement is supported by the existence of the sub-valent bismuth compound $Bi_{13}S_{18}I_2$ which exhibits $[Bi_2]^{4+}$dimers.[92] It is worth pointing out that the present compound, which represents the member $x = 2/3$ of a large series of closely related sulfides $(Cu_{1-x}\square_x)Pb_{1-x}Bi_{1+x}S_3$ with $0 \leq x \leq 1$, is paradigmatic for a broad family of *n*-type thermoelectric materials that are susceptible to optimization by varying the chemical composition, by controlling the order-disorder phenomena, and by tuning the carrier concentration through doping.

4. Methods Section

Reagents

High purity copper powder (Cu, Alfa Aesar, >99.99%), lead needles (Pb, Alfa Aesar, 99.99%), bismuth powder (Bi, Alfa Aesar, >99.5%), sulfur powder (S, Alfa Aesar, >99.99%) and bismuth (III) chloride ($BiCl_3$, Alfa Aesar, >99.99%) were used as precursors without further purification.

Synthesis

All samples were synthesized by mechanical alloying followed by spark plasma sintering. The high energy ball milling was executed in a Fritsch Pulverisette 7 Premium line planetary ball

mill operating at room temperature (RT) at a rotation speed of 600 rpm with the powder to ball ratio around 1:18. Typically, pristine $CuPbBi_5S_9$, $CuPbBi_5S_{9-z}Cl_z$ (where z = 0.03, 0.09 and 0.18) and $CuPb_{1-y}Bi_{5+y}S_9$ (where y = 0.05, 0.1, 0.25 and 0.5) were synthesized by milling stoichiometric amounts of Cu, Pb, Bi, $BiCl_3$ and S powders (total amount of 6g) for 6 hrs (12 cycles of 30 min with 1 min pause) under argon atmosphere. X-ray diffraction patterns of mechanically-alloyed powders after 30 min, 1 hr, 3 hrs and 6 hrs of milling are displayed in **Figure S20**. It can be observed that the crystallization of the phase is fast, as the main broad diffraction peaks corresponding to the $CuPbBi_5S_9$ phase appears after 30 min only.

Powders were then placed in graphite dies of 10 mm diameter and densified by spark plasma sintering (SPS-FCT HPD 25) at 723 K for 30 min under a pressure of 64 MPa with a heating and cooling rate of 50 and 20 K min^{-1}, respectively. This produced 10 mm diameter pellets, ca. 9 mm thick, with geometrical densities greater than 95% of the theoretical value.

X-ray powder diffraction

High-resolution X-ray powder diffraction (XRPD) data were collected at RT using a Bruker D8 Advance Vario 1 two-circle diffractometer (θ-2θ Bragg-Brentano mode) using Cu $K_{\alpha 1}$ radiation (λ = 1.5406 Å) with a Ge (111) monochromator (Johansson type) and a Lynx Eye detector. Synchrotron XRPD data of pristine $CuPbBi_5S_9$ sample were collected at RT on high-resolution XRD ID22 beamline at ESRF (Grenoble, France). ID22 is mounted on a set of undulators and work in Debye-Scherrer geometry with a high resolution setup, where the diffracted photons are collected using 8 crystal analyzer improving angular and energy resolution. The sample was finely ground and inserted in a borosilicate glass capillary of diameter 0.3 mm. Neutron powder diffraction (NPD) analyses were carried out at room temperature on the D2B high-flux and high-resolution powder diffractometer at the Institut Laue Langevin (Grenoble, France) on another batch of pristine $CuPbBi_5S_9$ sample prepared in

the same conditions. NPD data were collected at wavelength λ = 1.594 Å thanks to a germanium (335) monochromator and cylindrical sample-holder made of vanadium metal. Rietveld refinement performed by using the structural model of copper deficient aikinite (**Figure S21** and **Table S1**) confirms the absence of secondary phase and the Cu/vacancies disordered crystal structure. The diffraction data analyses were performed by Rietveld refinement using the FullProf and WinPlotr software packages.[93,94] The background contribution was refined with a polynomial function. Zero-point shift, peak shape parameters, asymmetry parameters, lattice parameters, fractional atomic coordinates and isotropic displacement parameters (*i.e.* Debye-Waller factors B_{iso}) were finally refined.

Transmission and scanning electron microscopy

The samples were prepared through gridding and ion-milling (Leica EM Res 102). Transmission electron microscopy (TEM) characterizations, including high-resolution TEM images (HRTEM), selected area electron diffraction (SAED) and high angle annular dark field (HAADF) images were obtained at 200 kV (Thermoscientific Talos F200S). Scanning electron micrographs and electron dispersive X-ray (EDX) spectroscopy analyses were collected using a JEOL JSM 7200F scanning electron microscope (SEM) equipped with EDX X-Flash Bruker detector.

Electrical and thermal properties measurements

The electrical resistivity (ρ) and Seebeck coefficient (S) were measured simultaneously from 2×3×10 mm^3 sintered ingots, from 300 K up to 700 K using an ULVAC-ZEM3 instrument under partial helium pressure. Note that some points are missing near RT for pristine, y = 0.05 and y = 0.1 samples due to their high electrical resistivity (not measurable with ZEM-3 system). A NETZSCH LFA-457 apparatus was used for measuring the thermal diffusivity

under argon flow. The thermal conductivity (κ) was determined as the product of the geometrical density, the thermal diffusivity, and the theoretical heat capacity using the Dulong−Petit approximation (0.25 J g^{-1} K^{-1} for $CuPbBi_5S_9$), in agreement with the experimental values (**Figure S22**). The lattice contribution to the thermal conductivity (κ_L) was determined by subtracting the estimated electronic component (κ_e) from the measured total thermal conductivity, κ. The electronic contribution, κ_e, was derived from the Wiedemann-Franz law, $= L\sigma T$, where the Lorenz number, L, was approximated from the Seebeck coefficient using the simplified expression $L = 1.5 + \exp(-|S|/116)$.[95] The estimated measurement uncertainties are 6% for the Seebeck coefficient, 8% for the electrical resistivity, 11% for the thermal conductivity, and 16% for the final figure of merit, ZT.[96] Room temperature Hall effect measurements were carried out using a Physical Properties Measurement System (PPMS, Quantum Design) under applied magnetic fields of up to 9T. To avoid under- or overestimation of ZT, all the measurements were performed along the direction perpendicular to the pressure direction. We have also measured the electrical resistivity, Seebeck coefficient and thermal conductivity in both directions (parallel and perpendicular to the pressure direction) on the $CuPbBi_5S_{9.91}Cl_{0.09}$ sample and confirmed that the properties are isotropic (**Figure S23**). This is in good agreement with the small size and isotropic shape of grains.

Specific heat C_p measurements were performed between 2 and 295 K by a conventional relaxation method using the dedicated ^{4}He option of the PPMS. Small polycrystalline pieces of approximately 15 mg were glued onto the sample holder by using a minute amount of Apiezon N grease. Details of the equation used to model the low-temperature specific heat data are given in the supporting information.

The longitudinal and transverse sound velocities were measured at 300 K using a pulse-echo method. A minute amount of grease was used to ensure a good contact between the sample and the piezoelectric transducers.

Optical measurements

The reflectance measurements were carried out on the ground powders of the $CuPbBi_5S_{9-z}Cl_z$ series in the spectral range between 200 to 2500 nm with a 1 nm step using a V-770 JASCO spectrophotometer equipped with an integrated reflectance sphere accessory. The optical band gaps (E_g) were determined from the absorption (K/S) data calculated from the raw reflectance data using the $K/S = (1-R)^2/(2R)$ Kubelka Munk transform. Indirect and direct band gaps were estimated from the Tauc plots (*i.e.* $(\alpha h\upsilon)^{1/n} = A(h\upsilon - E_g)$ with α the absorption coefficient of the material; A, a proportional constant and n equals to ½ and 2 for an indirect and the direct transition respectively) by considering the (K/S) Kubelka Munk function proportional to the absorption coefficient α (*i.e.* by considering the scattering coefficient S as constant with respect to wavelength).

Electrochemical measurements

Steady state and transient (photo)-electrochemical measurements were recorded using an Autolab PGSTAT204 (Metrohm AG) equipped with a FRA32M electrochemical impedance spectroscopy module. The electrochemical cell consisted of a three-electrode set-up, namely the $CuPbBi_5S_{9-z}Cl_z$ (z = 0, 0.09 and 0.18)-based electrodes as working electrode, a Pt wire as counter-electrode and a reference in Ag/AgCl, all dipped in a KCl (0.5 M in aqueous media) electrolyte. The pristine and $CuPbBi_5S_{9-z}Cl_z$ working electrodes were prepared from the dense pellets obtained by SPS and contacted in the backside with a copper wire using a carbon paste for a good electrical contact. This contact was then cured and sealed off with an epoxy resin

(CaldoFix-2kit, Struers), and the pellet surface was polished (SiC paper, grid 1200 and 4000) to obtain a smooth electrode surface. The photoelectrochemistry measurements were recorded under an MI-LED illuminator (Edmund Optics). The impedance spectra were measured in a frequency range from 100 Hz to 100 kHz. The Mott–Schottky analyses were recorded in a potential range of 0.2 to -0.6 vs Ag/AgCl at relatively high frequencies (1–10 kHz) allowing to neglect the diffusion phenomena. Thus, the interface semiconductor/electrolyte capacitance (C) was determined using a simplified Randles equivalent circuit by neglecting the Warburg component at high frequency. The C values for an applied potential were calculated from the constant phase element (CPE, $Z_{CPE} = 1/Q(j\omega)^{\alpha}$, where $0 < \alpha < 1$) reflecting the non-ideality of the interface capacitance using $C = (1/R_s + 1/R_{tc})^{(\alpha-1)/\alpha}Q^{1/\alpha}$. Flat band potentials ($V_{fb}$) were determined by extrapolation at $C^{-2} = 0$ from the Mott-Schottky plot (C_{SC}^{-2} vs V), which utilizes the Mott−Schottky equation (Equation 1) for a *n*-type semiconductor (Equation 1) and Fermi levels were approximated (E_F (eV) = - 4.5 – e.V_{fb} (RHE)). The charge carrier concentration N was determined from the value of the slope in considering a constant dielectric permittivity of 130 for the $CuPbBi_5S_{9-z}Cl_z$ (z = 0, 0.09 and 0.18) series:[97]

$$\frac{1}{C_{SC}^2} = \frac{2}{\varepsilon\varepsilon_0 e A^2 N}\left(V - V_{fb} - \frac{kT}{e}\right) \qquad \text{(Equation 1)}$$

where C_{SC} corresponds to the capacitance in the space charge region of the semiconductor, A the interfacial surface area between the semiconductor electrode and electrolyte, k the

Boltzmann constant, T the temperature, e the electron charge, ε_0 the vacuum permittivity, and ε the relative permittivity of the semiconductor. C_{SC}^{-2} was approximated to be C^{-2} due to the large capacitance of the Helmholtz layer, at the semiconductor surface in the electrolyte, in comparison to C_{SC}.

First-principles calculations

All the calculations were performed with the QUANTUM ESPRESSO[98] package as embedded in the high-throughput infrastructure AFLOWπ.[99] We used norm-conserving PBE pseudopotentials,[100] well converged basis sets corresponding to an energy cutoff of 150 Ry for the wave functions and 600 Ry for the charge density, and the ACBN0 functional approach[101] have been used to self-consistently determine the values for the Hubbard corrections for each atomic species of the material (U(Pb) = 0.005 eV, U(Cu) = 1.129 eV, U(Bi) = 0.043 eV, U(S) = 2.774 eV, and U(Cl) = 0.017 eV). To integrate over the Brillouin zone during the self-consistent cycle, a 3 × 9 × 1 and a 3 × 3 × 3 (shifted) grids were used for the ordered and fully disordered cells respectively (both cells have 64 atoms). The phonon calculations use ultrasoft pseudopotentials (energy cutoff of 60 Ry for the wave functions and 480 Ry for the charge) with the PBESol exchange-correlation functional.[102] Seebeck coefficient *S* and electrical conductivity σ were computed by solving Boltzmann transport equation within the constant relaxation time and the rigid band approximation as implemented in PAOFLOW.[103] Properties that depend on the crystalline momentum **k**, such as the band structure, has been reported only for the perfectly ordered gladite cell. We underline that for the disordered materials, due to the loss of periodicity, the Bloch theorem is no longer valid and the crystalline momentum **k** loses its significance; band structures are not properly representing the electronic structure of a disordered system due to the broken translational invariance. However, density of states (eDoS and vDoS) and transport coefficient do not

depend explicitly on the crystalline momentum (they are integrated quantities) and may represent faithfully realistic materials.

ASSOCIATED CONTENT

Supporting Information

Details of characterization, Rietveld fit profiles, transmission and scanning electron microscopy analyses, formation energy variations, additional electronic structure and transport data from first-principles, optical and electrochemical measurements, XRD data of mechanically-alloyed powders, NPD Rietveld refinement and results of pristine phase, equations used to model the low-temperature specific heat data, equations for calculating the Poison ratio (ν_p) and Grüneisen parameter (γ) and Debye temperature (Θ_D), equations for calculating the average sound velocity.

The Supporting Information is available free of charge on the ACS Publications website.

AUTHOR INFORMATION

Corresponding Author

* emmanuel.guilmeau@ensicaen.fr; pierric.lemoine@univ-rennes1.fr, forna1m@cmich.edu

Author Contributions

The manuscript was written through contributions of all authors. All authors have given approval to the final version of the manuscript.

Funding Sources

P.V. acknowledges The Leverhulme Trust for Research Project Grant (RPG-2019-288).

Notes

The authors declare no competing financial interest.

ACKNOWLEDGMENTS

The authors gratefully thank Christelle Bilot and Jerôme Lecourt for technical support. The authors acknowledge ESRF (Grenoble, France) and ILL (Grenoble, France) for provision of research facilities *(*doi:10.15151/ESRF-ES-404435424; doi:10.5291/ILL-DATA.5-23-752) and gratefully thank Andy Fitch, Catherine Dejoie, Vivian Nassif and Stanislav Savvin for technical assistance.

References

(1) DiSalvo, F. J. Thermoelectric Cooling and Power Generation. *Science.* **1999**, *285* (5428), 703–706.

(2) Bell, L. E. Cooling, Heating, Generating Power, and Recovering Waste Heat with Thermoelectric Systems. *Science.* **2008**, *321* (5895), 1457–1461.

(3) Tan, G.; Zhao, L. D.; Kanatzidis, M. G. Rationally Designing High-Performance Bulk Thermoelectric Materials. *Chem. Rev.* **2016**, *116* (19), 12123–12149.

(4) Ge, Z. H.; Zhao, L. D.; Wu, D.; Liu, X.; Zhang, B. P.; Li, J. F.; He, J. Low-Cost, Abundant Binary Sulfides as Promising Thermoelectric Materials. *Mater. Today* **2016**, *19* (4), 227–239.

(5) Powell, A. V. Recent Developments in Earth-Abundant Copper-Sulfide Thermoelectric Materials. *J. Appl. Phys.* **2019**, *126* (10), 100901.

(6) Guélou, G.; Lemoine, P.; Raveau, B.; Guilmeau, E. Recent Developments in High-Performance Thermoelectric Sulphides: An Overview of the Promising Synthetic Colusites. *J. Mater. Chem. C* **2021**, *9* (3), 773–795.

(7) Lemoine, P.; Guélou, G.; Raveau, B.; Guilmeau, E. Crystal Structure Classification of Copper-based Sulphides as a Tool for the Design of Inorganic Functional Materials. *Angew. Chemie Int. Ed.* **2021**. https://doi.org/10.1002/anie.202108686.

(8) Zhao, H.; Xu, X.; Li, C.; Tian, R.; Zhang, R.; Huang, R.; Lyu, Y.; Li, D.; Hu, X.; Pan, L.; Wang, Y. Cobalt-Doping in Cu_2SnS_3: Enhanced Thermoelectric Performance by Synergy of Phase Transition and Band Structure Modification. *J. Mater. Chem. A* **2017**, *5* (44), 23267–23275.

(9) Deng, T.; Xing, T.; Brod, M. K.; Sheng, Y.; Qiu, P.; Veremchuk, I.; Song, Q.; Wei, T.; Yang, J.; Snyder, G. J.; Grin, Y.; Chen, L.; Shi, X. Discovery of High-Performance Thermoelectric Copper Chalcogenide Using Modified Diffusion- Couple High-

Throughput Synthesis and Automated Histogram Analysis Technique. *Energy Environ. Sci.* **2020**, *13* (9), 3041–3053.

(10) Kumar, V. P.; Lemoine, P.; Carnevali, V.; Lebedev, O. I.; Boullay, P.; Raveau, B.; Al, R.; Al, R.; Fornari, M.; Prestipino, C.; Menut, D.; Candol, C.; Malaman, B.; Guilmeau, E. Ordered Sphalerite Derivative $Cu_5Sn_2S_7$: A Degenerate Semiconductor with High Carrier Mobility in the Cu–Sn–S Diagram. *J. Mater. Chem. A* **2021**, *9* (17), 10812–10826.

(11) Qiu, P.; Zhang, T.; Qiu, Y.; Shi, X.; Chen, L. Sulfide Bornite Thermoelectric Material: A Natural Mineral with Ultralow Thermal Conductivity. *Energy Environ. Sci.* **2014**, *7* (12), 4000–4006.

(12) Long, S. O. J.; Powell, A. V.; Vaqueiro, P.; Hull, S. High Thermoelectric Performance of Bornite through Control of the Cu(II) Content and Vacancy Concentration. *Chem. Mater.* **2018**, *30* (2), 456–464.

(13) He, Y.; Day, T.; Zhang, T.; Liu, H.; Shi, X.; Chen, L.; Snyder, G. J. High Thermoelectric Performance in Non-Toxic Earth- Abundant Copper Sulfide. *Adv. Mater.* **2014**, *26* (23), 3974–3978.

(14) Lu, X.; Morelli, D. T.; Xia, Y.; Zhou, F.; Ozolins, V.; Chi, H.; Zhou, X.; Uher, C. High Performance Thermoelectricity in Earth-Abundant Compounds Based on Natural Mineral Tetrahedrites. *Adv. Energy Mater.* **2013**, *3*, 342–348.

(15) Suekuni, K.; Tsuruta, K.; Kunii, M.; Nishiate, H.; Nishibori, E.; Maki, S.; Ohta, M.; Yamamoto, A.; Koyano, M. High-Performance Thermoelectric Mineral $Cu_{12-x}Ni_xSb_4S_{13}$ Tetrahedrite. *J. Appl. Phys.* **2013**, *113* (4), 043712.

(16) Suekuni, K.; Kim, F. S.; Takabatake, T. Tunable Electronic Properties and Low Thermal Conductivity in Synthetic Colusites $Cu_{26-x}Zn_xV_2M_6S_{32}$ ($x \leq 4$, M= Ge, Sn). *J. Appl. Phys.* **2014**, *116*, 063706.

(17) Bourgès, C.; Bouyrie, Y.; Supka, A. R.; Al, R.; Al, R.; Lemoine, P.; Lebedev, O. I.; Ohta, M.; Suekuni, K.; Nassif, V.; Hardy, V.; Daou, R.; Miyazaki, Y.; Fornari, M.; Guilmeau, E. High-Performance Thermoelectric Bulk Colusite by Process Controlled Structural Disordering. *J. Am. Chem. Soc.* **2018**, *140*, 2186–2195.

(18) Pavan Kumar, V.; Supka, A. R.; Lemoine, P.; Lebedev, O. I.; Raveau, B.; Suekuni, K.; Nassif, V.; Al Rahal Al Orabi, R.; Fornari, M.; Guilmeau, E. High Power Factors of Thermoelectric Colusites $Cu_{26}T_2Ge_6S_{32}$ (T = Cr, Mo, W): Toward Functionalization of the Conductive "Cu–S" Network. *Adv. Energy Mater.* **2019**, *9* (6), 1803249.

(19) Shen, X.; Xia, Y.; Yang, C.; Zhang, Z.; Li, S.; Tung, Y.; Benton, A.; Zhang, X.; Lu, X.; Wang, G.; He, J.; Zhou, X. High Thermoelectric Performance in Sulfide-Type Argyrodites Compound $Ag_8Sn(S_{1-x}Se_x)_6$ Enabled by Ultralow Lattice Thermal Conductivity and Extended Cubic Phase Regime. *Adv. Funct. Mater.* **2020**, *30*, 2000526.

(20) Tanimoto, T.; Suekuni, K.; Tanishita, T.; Usui, H.; Tadano, T.; Kamei, T.; Saito, H.; Nishiate, H.; Lee, C. H.; Kuroki, K. Enargite Cu_3PS_4 : A Cu – S-Based Thermoelectric Material with a Wurtzite-Derivative Structure. *Adv. Funct. Mater.* **2020**, *30* (22), 2000973–2000980.

(21) Guilmeau, E.; Maignan, A.; Wan, C.; Koumoto, K. On the Effects of Substitution, Intercalation, Non-Stoichiometry and Block Layer Concept in TiS_2 Based Thermoelectrics. *Phys. Chem. Chem. Phys.* **2015**, *17* (38), 24541–24555.

(22) Guilmeau, E.; Bréard, Y.; Maignan, A. Transport and Thermoelectric Properties in Copper Intercalated TiS_2 Chalcogenide. *Appl. Phys. Lett.* **2011**, *99* (5), 052107–052109.

(23) Xie, H.; Su, X.; Zheng, G.; Zhu, T.; Yin, K.; Yan, Y.; Uher, C.; Kanatzidis, M. G.; Tang, X. The Role of Zn in Chalcopyrite $CuFeS_2$: Enhanced Thermoelectric Properties

of $Cu_{1-x}Zn_xFeS_2$ with In Situ Nanoprecipitates. *Adv. Energy Mater.* **2017**, *7* (3), 1601299–1601312.

(24) Barbier, T.; Berthebaud, D.; Frésard, R.; Lebedev, O. I.; Guilmeau, E.; Eyert, V.; Maignan, A. Structural and Thermoelectric Properties of N-Type Isocubanite $CuFe_2S_3$. *Inorg. Chem. Front.* **2017**, *4* (3), 424–432.

(25) Chmielowski, R.; Bhattacharya, S.; Jacob, S.; Péré, D.; Jacob, A.; Moriya, K.; Delatouche, B.; Roussel, P.; Madsen, G.; Dennler, G. Strong Reduction of Thermal Conductivity and Enhanced Thermoelectric Properties in $CoSbS_{1-x}Se_x$ Paracostibite. *Sci. Rep.* **2017**, *7* (1), 1–11.

(26) Bourgès, C.; Lemoine, P.; Lebedev, O. I.; Daou, R.; Hardy, V.; Malaman, B.; Guilmeau, E. Low Thermal Conductivity in Ternary $Cu_4Sn_7S_{16}$ Compound. *Acta Mater.* **2015**, *97*, 180–190.

(27) Deng, T.; Wei, T. R.; Song, Q.; Xu, Q.; Ren, D.; Qiu, P.; Shi, X.; Chen, L. Thermoelectric Properties of N-Type $Cu_4Sn_7S_{16}$-Based Compounds. *RSC Adv.* **2019**, *9* (14), 7826–7832.

(28) Jemetio, J. P. F.; Zhou, P.; Kleinke, H. Crystal Structure, Electronic Structure and Thermoelectric Properties of $Cu_4Sn_7S_{16}$. *J. Alloys Compd.* **2006**, *417* (1–2), 55–59.

(29) Hashikuni, K.; Suekuni, K.; Watanabe, K.; Bouyrie, Y.; Ohta, M.; Ohtaki, M.; Takabatake, T. Carrier Concentration Tuning in Thermoelectric Thiospinel $Cu_2CoTi_3S_8$ by Oxidative Extraction of Copper. *J. Solid State Chem.* **2018**, *259*, 5–10.

(30) Bourgès, C.; Pavan, V.; Nagai, H.; Miyazaki, Y.; Raveau, B.; Guilmeau, E. Role of Cobalt for Titanium Substitution on the Thermoelectric Properties of the Thiospinel $CuTi_2S_4$. *J. Alloys Compd.* **2019**, *781*, 1169–1174.

(31) Nielsen, M. D.; Ozolins, V.; Heremans, J. P. Lone Pair Electrons Minimize Lattice Thermal Conductivity. *Energy Environ. Sci.* **2013**, *6* (2), 570–578.

(32) Vaqueiro, P.; Al Rahal Al Orabi, R.; Luu, S. D. N.; Guélou, G.; Powell, A. V.; Smith, R. I.; Song, J.-P.; Wee, D.; Fornari, M. The Role of Copper in the Thermal Conductivity of Thermoelectric Oxychalcogenides : Do Lone Pairs Matter? *Phys. Chem. Chem. Phys.* **2015**, *17* (47), 31735–31740.

(33) Biswas, K.; Zhao, L. D.; Kanatzidis, M. G. Tellurium-Free Thermoelectric: The Anisotropic n -Type Semiconductor Bi_2S_3. *Adv. Energy Mater.* **2012**, *2* (6), 634–638.

(34) Guin, S. N.; Biswas, K. Cation Disorder and Bond Anharmonicity Optimize the Thermoelectric Properties in Kinetically Stabilized Rocksalt $AgBiS_2$ Nanocrystals. *Chem. Mater.* **2013**, *25* (15), 3225–3231.

(35) Tan, G.; Hao, S.; Zhao, J.; Wolverton, C.; Kanatzidis, M. G. High Thermoelectric Performance in Electron-Doped $AgBi_3S_5$ with Ultralow Thermal Conductivity. *J. Am. Chem. Soc.* **2017**, *139* (18), 6467–6473.

(36) Bhui, A.; Dutta, M.; Mukherjee, M.; Rana, K. S.; Singh, A. K.; Soni, A.; Biswas, K. Ultralow Thermal Conductivity in Earth-Abundant $Cu_{1.6}Bi_{4.8}S_8$: Anharmonic Rattling of Interstitial Cu. *Chem. Mater.* **2021**, *33* (8), 2993–3001.

(37) Labégorre, J. B.; Virfeu, A.; Bourhim, A.; Willeman, H.; Barbier, T.; Appert, F.; Juraszek, J.; Malaman, B.; Huguenot, A.; Gautier, R.; Nassif, V.; Lemoine, P.; Prestipino, C.; Elkaim, E.; Pautrot-d'Alençon, L.; Le Mercier, T.; Maignan, A.; Al Rahal Al Orabi, R.; Guilmeau, E. XBi_4S_7 (X = Mn, Fe): New Cost-Efficient Layered n-Type Thermoelectric Sulfides with Ultralow Thermal Conductivity. *Adv. Funct. Mater.* **2019**, *29* (48), 1904112–1904124.

(38) Xi, M.; Zhu, H.; Wu, H.; Yang, Y.; Yan, Y.; Wang, G.; Wang, G.; Li, J. Y.; Lu, X.; Zhou, X. Thermoelectricity of N-Type $MnBi_4S_{7-7x}Se_{7x}$ Solid Solution. *Chem. Eng. J.* **2020**, *396*, 125219.

(39) Liang, H.; Guo, J.; Zhou, Y. X.; Wang, Z. Y.; Feng, J.; Ge, Z. H. $CuPbBi_5S_9$

Thermoelectric Material with an Intrinsic Low Thermal Conductivity: Synthesis and Properties. *J. Mater.* **2021**, *13*. https://doi.org/10.1016/j.jmat.2021.03.016.

(40) Ohmasa, M.; Nowacki, W. A Redetermination of the Crystal Structure of Aikinite [$BiS_2|S|Cu^{IV}Pb^{VII}$]. *Z. Krist.* **1970**, *132*, 71–86.

(41) Kohatsu, I.; Wuensch, B. J. The Crystal Structure of Aikinite, $PbCuBiS_3$. *Acta Crystallogr. Sect. B Struct. Crystallogr. Cryst. Chem.* **1971**, *27* (6), 1245–1252.

(42) Mumme, W. G.; Watts, J. A. Pekoite,$CuPbBi_{11}S_{18}$, A New Member of the Bismuthinite-Aikinite Mineral Series: Its Crstal Struture and Relationship with Naturally- and Synhthetically-Formed Members. *Can. Mineral.* **1976**, *14*, 322–333.

(43) Kupčík, V.; Veselá-Nováková, L. Zur Kristallstruktur Des Bismuthinits, Bi_2S_3. *Tschermaks Mineral. und Petrogr. Mitteilungen* **1970**, *14* (1), 55–59.

(44) Lundegaard, L. F.; Makovicky, E.; Boffa-Ballaran, T.; Balic-Zunic, T. Crystal Structure and Cation Lone Electron Pair Activity of Bi_2S_3 between 0 and 10 GPa. *Phys. Chem. Miner.* **2005**, *32* (8), 578–584.

(45) Pring, A. Annealing of Synthetic Hammarite, $Cu_2Pb_2Bi_4S_9$, and the Nature of Cation-Ordering Processes in the Bismuthinite-Aikinite Series. *Am. Mineral.* **1995**, *80* (11), 1166–1173.

(46) Petříček, V.; Makovicky, E. Interpretation of Selected Structures of the Bismuthinite - Aikinite Series as Commensurately Modulated Structures. *Can. Mineral.* **2006**, *44* (1), 189–206.

(47) Syneˇcek, V.; Hybler, J. The Crystal Structure of Krupkaite, $CuPbBi_3S_6$, and of Gladite, $CuPbBi_5S_9$, and the Classification of Superstructures in the Bismuthinite–Aikinite Group. *Neues Jahrb. Miner. Monatsh.* **1974**, 541–560.

(48) Kohatsu, I.; Wuensch, B. J. The Crystal Structure of Gladite, $PbCuBi_5S_9$, a Superstructure Intermediate in the Series Bi_2S_3–$PbCuBiS_3$ (Bismuthinite–Aikinite).

Acta Crystallogr. Sect. B Struct. Crystallogr. Cryst. Chem. **1976**, *32* (8), 2401–2409.

(49) Balić- Žunić, T.; Topa, D.; Makovicky, E. The Crystal Structure of Emilite, $Cu_{10.7}Pb_{10.7}Bi_{21.3}S_{48}$, the Second 45 Å Derivative of the Bismuthinite-Aikinite Solid-Solution Series. *Can. Mineral.* **2002**, *40* (1), 239–245.

(50) Topa, D.; Makovicky, E.; Balić-Žunić, T. The Structural Role of Excess Cu and Pb in Gladite and Krupkaite Based on New Refinements of Their Structure. *Can. Mineral.* **2002**, *40* (4), 1147–1159.

(51) Topa, D.; Balić-Žunić, T.; Makovicky, E. The Crystal Structure of $Cu_{1.6}Pb_{1.6}Bi_{6.4}S_{12}$, a New 44.8 Å Derivative of the Bismuthinite-Aikinite Solid-Solution Series. *Can. Mineral.* **2000**, *38*, 611–616.

(52) Chen, T. T.; Kirchner, E.; Paar, W. Friedrichite, $Cu_5Pb_5Bi_7S_{18}$, A New Member of the Aikinite-Bismuthinite Series. *Can. Mineral.* **2015**, *16* (2), 127–130.

(53) Horruchi, H.; Wuensch, B. J. The Ordering Scheme for Metal Atoms in the Crystal Structure of Hammarite, $Cu_2Pb_2Bi_4S_9$. *Can. Mineral.* **1976**, *14* (4), 536–539.

(54) Horiuchi, H.; Wuensch, B. J. Lindstromite, $Cu_3Pb_3Bi_7S_{15}$: Its Space Group and Ordering Scheme for Metal Atoms in the Crystal Structure. *Can. Mineral.* **1977**, *15* (4), 527–535.

(55) Topa, D.; Petříček, V.; Dušek, M.; Makovicky, E.; Balić-Žunić, T. Simultaneous Refinement of Two Components of an Exsolution Intergrowth: Crystal Structures of the Lindströmite - Krupkaite Pair. *Can. Mineral.* **2008**, *46* (2), 525–539.

(56) Makovicky, E.; Topa, D.; Balić-Žunić, T. The Crystal Structure of Paarite, the Newly Discovered 56 Å Derivative of the Bismuthinite-Aikinite Solid-Solution Series. *Can. Mineral.* **2001**, *39* (5), 1377–1382.

(57) Kanishcheva, A. S.; Mikhailov, Y. N.; Trippel, A. F. Refinement of the Crystal Structure of Synthetic Bismuthinite. *Inorg. Mater.* **1981**, *17* (11), 1466–1468.

(58) Burstein, E. Anomalous Optical Absorption Limit in InSb. *Phys. Rev.* **1954**, *93* (3), 632–633.

(59) Moss, T. S. The Interpretation of the Properties of Indium Antimonide. *Proc. Phys. Soc. Sect. B* **1954**, *67* (10), 775–782.

(60) Mumme, W. G. The Crystal Structure of Krupkaite, $CuPbBi_3S_6$, from the Juno Mine at - Tennant Creek, Northern Territory, Australia. *Am. Mineral.* **1975**, *60* (3–4), 300–308.

(61) Dutta, M.; Matteppanavar, S.; Prasad, M. V.D.; Pandey, J.; Warankar, A.; Mandal, P.; Soni, A.; Waghmare, U. V.; Biswas, K. Ultralow Thermal Conductivity in Chain-like TlSe Due to Inherent Tl^+ Rattling. *J. Am. Chem. Soc.* **2019**, *141* (51), 20293–20299.

(62) Misra, S.; Barreteau, C.; Crivello, J.-C.; Giordano, V. M.; Castellan, J.-P.; Sidis, Y.; Levinský, P.; Hejtmánek, J.; Malaman, B.; Dauscher, A.; Lenoir, B.; Candolfi, C.; Pailhès, S. Reduced Phase Space of Heat-Carrying Acoustic Phonons in Single-Crystalline InTe. *Phys. Rev. Res.* **2020**, *2* (4), 043371–043387.

(63) Jana, M. K.; Pal, K.; Warankar, A.; Mandal, P.; Waghmare, U. V.; Biswas, K. Intrinsic Rattler-Induced Low Thermal Conductivity in Zintl Type $TlInTe_2$. *J. Am. Chem. Soc.* **2017**, *139* (12), 4350–4353.

(64) Lin, W.; He, J.; Su, X.; Zhang, X.; Xia, Y.; Bailey, T. P.; Stoumpos, C. C.; Tan, G.; Rettie, A. J. E.; Chung, D. Y.; Dravid, V. P.; Uher, C.; Wolverton, C.; Kanatzidis, M. G. Ultralow Thermal Conductivity, Multiband Electronic Structure and High Thermoelectric Figure of Merit in TlCuSe. *Adv. Mater.* **2021**, *33* (44) 2104908–2104918.

(65) Mukhopadhyay, S.; Parker, D. S.; Sales, B. C.; Puretzky, A. A.; McGuire, M. A.; Lindsay, L. Two-Channel Model for Ultralow Thermal Conductivity of Crystalline Tl_3VSe_4. *Science.* **2018**, *360* (6396), 1455–1458.

(66) Suekuni, K.; Tanaka, H. I.; Kim, F. S.; Umeo, K.; Takabatake, T. Glasslike versus

Crystalline Thermophysical Properties of the Cu-S Based Minerals: Tetrahedrite and Colusite. *J. Phys. Soc. Japan* **2015**, *84* (10), 103601–103604.

(67) Lara-Curzio, E.; May, A. F.; Delaire, O.; McGuire, M. A.; Lu, X.; Liu, C. Y.; Case, E. D.; Morelli, D. T. Low-Temperature Heat Capacity and Localized Vibrational Modes in Natural and Synthetic Tetrahedrites. *J. Appl. Phys.* **2014**, *115* (19), 193515–193521.

(68) Candolfi, C.; Guélou, G.; Bourgès, C.; Supka, A. R.; Al Rahal Al Orabi, R.; Fornari, M.; Malaman, B.; Le Caër, G.; Lemoine, P.; Hardy, V.; Zanotti, J. M.; Chetty, R.; Ohta, M.; Suekuni, K.; Guilmeau, E. Disorder-Driven Glasslike Thermal Conductivity in Colusite $Cu_{26}V_2Sn_6S_{32}$ Investigated by Mössbauer Spectroscopy and Inelastic Neutron Scattering. *Phys. Rev. Mater.* **2020**, *4* (2), 25404–25413.

(69) Mutka, H.; Koza, M. M.; Johnson, M. R.; Hiroi, Z.; Yamaura, J. I.; Nagao, Y. Generalized Density-of-States and Anharmonicity of the Low-Energy Phonon Bands from Coherent Inelastic Neutron Scattering Response in the Pyrochlore Osmates a Os_2O_6 (A=K, Rb, Cs). *Phys. Rev. B - Condens. Matter Mater. Phys.* **2008**, *78* (10), 104307–104313.

(70) Koza, M. M.; Mutka, H.; Okamoto, Y.; Yamaura, J. I.; Hiroi, Z. On the Microscopic Dynamics of the "Einstein Solids" AlV_2Al_{20} and GaV_2Al_{20}, and of YV_2Al_{20}: A Benchmark System for "Rattling" Excitations. *Phys. Chem. Chem. Phys.* **2015**, *17* (38), 24837–24850.

(71) Zhang, J.; Roth, N.; Tolborg, K.; Takasashi, S.; Song, L.; Bondesgaad, M.; Nishibori, E.; Iversen, B. B. Direct Observation of One-Dimensional Disordered Diffusion Channel in a Chain-like Thermoelectric with Ultralow Thermal Conductivity. *Nat. Commun.* **2021**, *12* (1), 6709–6718..

(72) Pal, K.; Xia, Y.; Wolverton, C. Microscopic Mechanism of Unusual Lattice Thermal Transport in $TlInTe_2$. *npj Comput. Mater.* **2021**, *7* (1). https://doi.org/10.1038/s41524-

020-00474-5.

(73) Xia, Y.; Ozolins, V.; Wolverton, C. Microscopic Mechanisms of Glasslike Lattice Thermal Transport in Cubic $Cu_{12}Sb_4S_{13}$ Tetrahedrites. *Phys. Rev. Lett.* **2020**, *125* (8), 085901–085907.

(74) Cahill, D. G.; Watson, S. K.; Pohl, R. O. Lower Limit to the Thermal Conductivity of Disordered Crystals. *Phys. Rev.* **1992**, *46* (10), 6131–6140.

(75) Zhao, L. D.; He, J.; Wu, C. I.; Hogan, T. P.; Zhou, X.; Uher, C.; Dravid, V. P.; Kanatzidis, M. G. Thermoelectrics with Earth Abundant Elements: High Performance p-Type PbS Nanostructured with SrS and CaS. *J. Am. Chem. Soc.* **2012**, *134* (18), 7902–7912.

(76) Avila, M. A.; Suekuni, K.; Umeo, K.; Fukuoka, H.; Yamanaka, S.; Takabatake, T. Glasslike versus Crystalline Thermal Conductivity in Carrier-Tuned $Ba_8Ga_{16}X_{30}$ Clathrates (X=Ge,Sn). *Phys. Rev. B - Condens. Matter Mater. Phys.* **2006**, *74* (12), 125109–125116.

(77) Koza, M. M.; Leithe-Jasper, A.; Rosner, H.; Schnelle, W.; Mutka, H.; Johnson, M. R.; Krisch, M.; Capogna, L.; Grin, Y. Vibrational Dynamics of the Filled Skutterudites $M_{1-x}Fe_4Sb_{12}$ (M=Ca, Sr, Ba, and Yb): Temperature Response, Dispersion Relation, and Material Properties. *Phys. Rev. B - Condens. Matter Mater. Phys.* **2011**, *84* (1), 014306–014317.

(78) Troć, R.; Wawryk, R.; Gajek, Z.; Pasturel, M.; Samsel-Czekała, M. Comparative Studies of the Cage Systems $ThFe_2Al_{10}$ and UFe_2Al_{10}. *J. Alloys Compd.* **2017**, *727*, 1302–1313.

(79) Morelli, D. T.; Jovovic, V.; Heremans, J. P. Intrinsically Minimal Thermal Conductivity in Cubic I-V-VI_2 Semiconductors. *Phys. Rev. Lett.* **2008**, *101* (3), 035901.

(80) Liu, X.; Wang, D.; Wu, H.; Wang, J.; Zhang, Y.; Wang, G.; Pennycook, S. J.; Zhao, L.

D. Intrinsically Low Thermal Conductivity in $BiSbSe_3$: A Promising Thermoelectric Material with Multiple Conduction Bands. *Adv. Funct. Mater.* **2019**, *29* (3), 1806558–1806566.

(81) Xiao, Y.; Chang, C.; Pei, Y.; Wu, D.; Peng, K.; Zhou, X.; Gong, S.; He, J.; Zhang, Y.; Zeng, Z.; Zhao, L. D. Origin of Low Thermal Conductivity in SnSe. *Phys. Rev. B* **2016**, *94* (12), 125203.

(82) Gao, X.; Zhou, M.; Cheng, Y.; Ji, G. First-Principles Study of Structural, Elastic, Electronic and Thermodynamic Properties of Topological Insulator Bi_2S_3 under Pressure. *Philos. Mag.* **2016**, *96* (2), 208–222.

(83) Cai, F.; Dong, R.; Sun, W.; Lei, X.; Yu, B.; Chen, J.; Yuan, L.; Wang, C.; Zhang, Q. $Pb_mBi_2S_{3+m}$ Homologous Series with Low Thermal Conductivity Prepared by the Solution-Based Method as Promising Thermoelectric Materials. *Chem. Mater.* **2021**, *33* (15), 6003–6011.

(84) Chasmar, R. P.; Stratton, R. The Thermoelectric Figure of Merit and Its Relation to Thermoelectric Generators. *J. Eletronics Control* **1959**, *7*, 52–72.

(85) Mahan, G. D.; Sofot, J. The Best Thermoelectric. *Proc. Natl. Acad. Sci. United States Am.* **1996**, *93*, 7436–7439.

(86) Wang, H.; Pei, Y.; Lalonde, A. D.; Snyder, G. J. Material Design Considerations Based on Thermoelectric Quality Factor. *Thermoeletric Nanomater. Mater. Des. Appl.* **2013**, 3–32.

(87) Zhang, X.; Bu, Z.; Shi, X.; Chen, Z.; Lin, S.; Shan, B.; Wood, M.; Snyder, A. H.; Chen, L.; Snyder, G. J.; Pei, Y. Electronic Quality Factor for Thermoelectrics. *Sci. Adv.* **2020**, *6,* 6–11.

(88) Hong, M.; Lyu, W.; Wang, Y.; Zou, J.; Chen, Z. Establishing the Golden Range of Seebeck Coefficient for Maximizing Thermoelectric Performance. *J. Am. Chem. Soc.*

2020, *142* (5), 2672−2681.

(89) Ahn, J. Y.; Hwang, J. Y.; Ryu, B. K.; Oh, M. W.; Lee, K. H.; Kim, S. W. Importance of Crystal Chemistry with Interstitial Site Determining Thermoelectric Transport Properties in Pavonite Homologue Cu-Bi-S Compounds. *CrystEngComm* **2016**, *18* (8), 1453–1461.

(90) Li, J.; Zhou, Y.; Hao, S.; Zhang, T.; Wolverton, C.; Zhao, J.; Zhao, L. D. Thermoelectric Material $SnPb_2Bi_2S_6$: The ^{4,4}L Member of Lillianite Homologous Series with Low Lattice Thermal Conductivity. *Inorg. Chem.* **2019**, *58* (2), 1339–1348.

(91) Zhao, J.; Hao, S.; Islam, S. M.; Chen, H.; Tan, G.; Ma, S.; Wolverton, C.; Kanatzidis, M. G. Six Quaternary Chalcogenides of the Pavonite Homologous Series with Ultralow Lattice Thermal Conductivity. *Chem. Mater.* **2019**, *31* (9), 3430–3439.

(92) Groom, R.; Jacobs, A.; Cepeda, M.; Drummey, R.; Latturner, S. E. $Bi_{13}S_{18}I_2$: (Re)Discovery of a Subvalent Bismuth Compound Featuring $[Bi_2]^{4+}$ Dimers Grown in Sulfur/Iodine Flux Mixtures. *Chem. Mater.* **2017**, *29* (7), 3314–3323. h

(93) Rodríguez-Carvajal, J. Recent Advances in Magnetic Structure Determination by Neutron Powder Diffraction. *Phys. B Condens. Matter* **1993**, *192*, 55–69.

(94) Roisnel, T.; Rodríguez-Carvajal, J. WinPLOTR: A Windows Tool for Powder Diffraction Pattern Analysis. *Mater. Sci. Forum* **2001**, *378* (1), 118–123.

(95) Kim, H. S.; Gibbs, Z. M.; Tang, Y.; Wang, H.; Snyder, G. J. Characterization of Lorenz Number with Seebeck Coefficient Measurement. *APL Mater.* **2015**, *3* (4), 041506–041510.

(96) Alleno, E.; Bérardan, D.; Byl, C.; Candolfi, C.; Daou, R.; Decourt, R.; Guilmeau, E.; Hébert, S.; Hejtmanek, J.; Lenoir, B.; Masschelein, P.; Ohorodnichuk, V.; Pollet, M.; Populoh, S.; Ravot, D.; Rouleau, O.; Soulier, M. Invited Article: A Round Robin Test of the Uncertainty on the Measurement of the Thermoelectric Dimensionless Figure of

Merit of $Co_{0.97}Ni_{0.03}Sb_3$. *Rev. Sci. Instrum.* **2015**, *86* (1), 011301–011309.

(97) Brilingas, A.; Grigas, J.; Bendorius, R. Investigation of the Bi_2S_3-$CuPbBi_5S_9$ Solid Solution . *Lith. J. Phys.* **1977**, *17*, 501–506.

(98) Giannozzi, P.; Baroni, S.; Bonini, N.; Calandra, M.; Car, R.; Cavazzoni, C.; Cherubini, M.; Ceresoli, D.; Chiarotti, G. L.; Cococcioni, M.; Dabo, I.; Corso, A. D.; Gironcoli, S. De; Fabris, S.; Fratesi, G.; Gebauer, R.; Gerstmann, U.; Gougoussis, C.; Kokalj, A.; Lazzeri, M.; Martin-samos, L.; Marzari, N.; Mauri, F.; Mazzarello, R.; Paolini, S.; Pasquarello, A.; Paulatto, L.; Sbraccia, C.; Scandolo, S.; Sclauzero, G.; Seitsonen, A. P.; Smogunov, A.; Umari, P.; Wentzcovitch, R. M. QUANTUM ESPRESSO : A Modular and Open-Source Software Project for Quantum Simulations of Materials. *J. Phys. Condens Matter* **2009**, *21* (39), 395502.

(99) Supka, A. R.; Lyons, T. E.; Liyanage, L.; Amico, P. D.; Al Rahal Al Orabi, R.; Mahatara, S.; Gopal, P.; Toher, C.; Ceresoli, D.; Calzolari, A.; Curtarolo, S.; Nardelli, M. B.; Fornari, M. AFLOW Π : A Minimalist Approach to High-Throughput Ab Initio Calculations Including the Generation of Tight-Binding Hamiltonians. *Comput. Mater. Sci.* **2017**, *136*, 76–84.

(100) Hamann, D. R. Optimized Norm-Conserving Vanderbilt Pseudopotentials. *Phys. Rev. B* **2013**, *88* (8), 085117.

(101) Agapito, L. A.; Curtarolo, S.; Nardelli, M. B. Reformulation of DFT + U as a Pseudohybrid Hubbard Density Functional for Accelerated Materials Discovery. *Phys. Rev. X* **2015**, *5* (1), 011006.

(102) Perdew, J. P.; Ruzsinszky, A.; Csonka, I. G.; Vydrov, O. A.; Scuseria, G. E.; Constantin, L. A.; Zhou, X.; Burke, K. Restoring the Density-Gradient Expansion for Exchange in Solids and Surfaces. *Phys. Rev. Lett.* **2008**, *100* (13), 136406.

(103) Buongiorno, M.; Cerasoli, F. T.; Costa, M.; Curtarolo, S.; Gennaro, R. De; Fornari, M.;

Liyanage, L.; Supka, A. R.; Wang, H. PAOFLOW : A Utility to Construct and Operate on Ab Initio Hamiltonians from the Projections of Electronic Wavefunctions on Atomic Orbital Bases , Including Characterization of Topological Materials. *Comput. Mater. Sci.* **2018**, *143*, 462–472.

For Table of Contents Only